Universität Potsdam – Institut für Erd- und Umweltwissenschaften
Karl-Liebknecht-Strasse 24, 14476 Potsdam, Deutschland

Improving statistical seismicity models

Dissertation zur Erlangung des akademischen Grades
"doctor rerum naturalium" (Dr. rer. nat.)
in der Wissenschaftsdisziplin "Geophysik"

eingereicht an der Mathematisch-Naturwissenschaftlichen
Fakultät der Universität Potsdam

von
Christoph Bach

29. August 2013

Betreuer:
PD Dr. Sebastian Hainzl, Helmholtz-Zentrum Potsdam, Deutsches GeoForschungsZentrum

Published online at the
Institutional Repository of the University of Potsdam:
URL http://opus.kobv.de/ubp/volltexte/2014/7059/
URN urn:nbn:de:kobv:517-opus-70591
http://nbn-resolving.de/urn:nbn:de:kobv:517-opus-70591

Eidesstattliche Versicherung

Ich erkläre hiermit, dass ich die vorliegende Arbeit selbständig und ohne Benutzung anderer als der angegebenen Hilfsmittel angefertigt habe. Aus fremden Quellen direkt oder indirekt übernommene Gedanken sind als solche kenntlich gemacht. Diese Arbeit hat in gleicher oder ähnlicher Form noch keiner anderen Prüfungsbehörde vorgelegen.

Ort, Datum **Unterschrift (Vor- und Zuname)**

Abstract

Several mechanisms are proposed to be part of the earthquake triggering process, including static stress interactions and dynamic stress transfer. Significant differences of these mechanisms are particularly expected in the spatial distribution of aftershocks. However, testing the different hypotheses is challenging because it requires the consideration of the large uncertainties involved in stress calculations as well as the appropriate consideration of secondary aftershock triggering which is related to stress changes induced by smaller pre- and aftershocks.

In order to evaluate the forecast capability of different mechanisms, I take the effect of smaller–magnitude earthquakes into account by using the epidemic type aftershock sequence (ETAS) model where the spatial probability distribution of direct aftershocks, if available, is correlated to alternative source information and mechanisms. Surface shaking, rupture geometry, and slip distributions are tested. As an approximation of the shaking level, ShakeMaps are used which are available in near real-time after a mainshock and thus could be used for first-order forecasts of the spatial aftershock distribution. Alternatively, the use of empirical decay laws related to minimum fault distance is tested and Coulomb stress change calculations based on published and random slip models. For comparison, the likelihood values of the different model combinations are analyzed in the case of several well-known aftershock sequences (1992 Landers, 1999 Hector Mine, 2004 Parkfield).

The tests show that the fault geometry is the most valuable information for improving aftershock forecasts. Furthermore, they reveal that static stress maps can additionally improve the forecasts of off–fault aftershock locations, while the integration of ground shaking data could not upgrade the results significantly.

In the second part of this work, I focused on a procedure to test the information content of inverted slip models. This allows to quantify the information gain if this kind of data is included in aftershock forecasts. For this purpose, the ETAS

model based on static stress changes, which is introduced in part one, is applied. The forecast ability of the models is systematically tested for several earthquake sequences and compared to models using random slip distributions. The influence of subfault resolution and segment strike and dip is tested. Some of the tested slip models perform very good, in that cases almost no random slip models are found to perform better. Contrastingly, for some of the published slip models, almost all random slip models perform better than the published slip model. Choosing a different subfault resolution hardly influences the result, as long the general slip pattern is still reproducible. Whereas different strike and dip values strongly influence the results depending on the standard deviation chosen, which is applied in the process of randomly selecting the strike and dip values.

Zusammenfassung

Verschiedene Mechanismen werden für das Triggern von Erdbeben verantwortlich gemacht, darunter statische Spannungsänderungen und dynamischer Spannungstransfer. Deutliche Unterschiede zwischen diesen Mechanismen werden insbesondere in der räumlichen Nachbebenverteilung erwartet. Es ist allerdings schwierig diese Hypothesen zu überprüfen, da die großen Unsicherheiten der Spannungsberechnungen berücksichtigt werden müssen, ebenso wie das durch lokale sekundäre Spannungsänderungen hervorgerufene initiieren von sekundären Nachbeben.

Um die Vorhersagekraft verschiedener Mechanismen zu beurteilen habe ich die Effekte von Erdbeben kleiner Magnitude durch Benutzen des "epidemic type aftershock sequence" (ETAS) Modells berücksichtigt. Dabei habe ich die Verteilung direkter Nachbeben, wenn verfügbar, mit alternativen Herdinformationen korreliert. Bodenbewegung, Bruchgeometrie und Slipmodelle werden getestet. Als Aproximation der Bodenbewegung werden ShakeMaps benutzt. Diese sind nach großen Erdbeben nahezu in Echtzeit verfügbar und können daher für vorläufige Vorhersagen der räumlichen Nachbebenverteilung benutzt werden. Alternativ können empirische Beziehungen als Funktion der minimalen Distanz zur Herdfläche benutzt werden oder Coulomb Spannungsänderungen basierend auf publizierten oder zufälligen Slipmodellen. Zum Vergleich werden die Likelihood Werte der Hybridmodelle im Falle mehrerer bekannter Nachbebensequenzen analysiert (1992 Landers, 1999 Hector Mine, 2004 Parkfield).

Die Tests zeigen, dass die Herdgeometrie die wichtigste Zusatzinformation zur Verbesserung der Nachbebenvorhersage ist. Des Weiteren können statische Spannungsänderungen besonders die Vorhersage von Nachbeben in größerer Entfernung zur Bruchfläche verbessern, wohingegen die Einbeziehung von Bodenbewegungskarten die Ergebnisse nicht wesentlich verbessern konnte.

Im zweiten Teil meiner Arbeit führe ich ein neues Verfahren zur Untersuchung des Informationsgehaltes von invertierten Slipmodellen ein. Dies ermöglicht die Quantifizierung des Informationsgewinns, der durch Einbeziehung dieser Daten in Nachbebenvorhersagen entsteht. Hierbei wird das im ersten Teil eingeführte erweiterte ETAS Modell benutzt, welches statische Spannungsänderung zur Vorhersage der räumlichen Nachbebenverteilung benutzt.

Die Vorhersagekraft der Modelle wird systematisch anhand mehrerer Erdbebensequenzen untersucht und mit Modellen basierend auf zufälligen Slipverteilungen verglichen. Der Einfluss der Veränderung der Auflösung der Slipmodelle, sowie Streich- und Fallwinkel der Herdsegmente wird untersucht. Einige der betrachteten Slipmodelle korrelieren sehr gut, in diesen Fällen werden kaum zufällige Slipmodelle gefunden, welche die Nachbebenverteilung besser erklären. Dahingegen korrelieren bei einigen Beispielen nahezu alle zufälligen Slipmodelle besser als das publizierte Modell. Das Verändern der Auflösung der Bewegungsmodelle hat kaum Einfluss auf die Ergebnisse, solange die allgemeinen Slipmuster noch reproduzierbar sind, d.h. ein bis zwei größere Slipmaxima pro Segment. Dahingegen beeinflusst eine zufallsbasierte Änderung der Streich- und Fallwinkel der Segmente die Resultate stark, je nachdem welche Standardabweichung gewählt wurde.

Acknowledgments

This work was supported by PROGRESS, the Potsdam Research Cluster for Georisk Analysis, Environmental Change and Sustainability, and the GFZ German Research Centre for Geosciences. I am very thankful for the financial support, the excellent scientific environment at GFZ and especially to my supervisor Dr. Sebastian Hainzl, who always supported me with advices in scientific and non–scientific manner and enabled me to present my results on a number of international conferences.

I would like to thank Prof. Sandy Steacy, Prof. Frank Krüger and Dr. Gert Zöller for fruitful discussions during conferences and project meetings. And I am very much indebted to them to agree being reviewers of my thesis.

GFZ Section 2.1 was the best place I can imagine to stay to do my PhD, I felt very comfortable on the professional and personal level. Special thanks goes to my colleagues and friends Camilla Cattania, Katrin Kieling and Olga Zakharova, who shared the office with me for several years. Also special thanks to Hannes Bathke, Manoochehr Shirzaei and Medhi Nikkhoo for their friendship, all the research related and not research related discussions, the evening beers and the never ending motivation to push forward the frontiers of science.

Finally, and most importantly, I want to sincerely thank my family, who always supported me in all my decisions.

Contents

List of Figures

1 Introduction

Aftershock clustering in space and time is a dominating feature of seismic activity and therefore important for understanding and testing earthquake physics as well as for seismic hazard assessment. In particular, already by the mainshock damaged buildings are much more vulnerable to collapse if smaller magnitude aftershocks occur. Aftershocks are triggered earthquakes in a sequence of events that occur after a previous event, the so called mainshock. The exact timing of individual events is random, but an increased rate is observed that is temporally and spatially correlated with the mainshock. It seems to be clear that the mainshock induced stress and state changes are the origin of aftershock activity, however the main triggering mechanism is still controversially discussed. There are several mechanisms proposed to be responsible for triggering aftershocks including static and dynamic stress changes (Harris 1998), afterslip (Perfettini and Avouac 2007) and poro-elastic effects (Nur and Booker 1972, Cocco and Rice 2002). These mechanisms differ in particular in predicting the spatial aftershock distribution. A comparative evaluation and application of the models is challenging, because they all need additional information and parameter settings.

A purely statistical model is the *Epidemic Type Aftershock Sequence* model (ETAS), which combines main empirical features, in particular Omori–Utsu type time decay and the exponential dependence of the aftershock productivity on the mainshock magnitude. The ETAS model provides an estimate of the temporal and spatial aftershock distribution. However, it predicts an isotropic (i.e. rotation invariant) spatial clustering, which clearly contradicts the elongated shape of fault

zones and aftershock activity. The aim is to develop hybrid models based on the empirical ETAS model and additional source information.

To improve spatial aftershock forecast it is necessary to use additional inputs which are quickly available after large events. ShakeMaps are available in near real time and provide observed surface ground motions following large earthquakes. Peak ground velocity is typically highest close to the ruptured fault and is proposed to be the triggering mechanism for aftershocks (van der Elst and Brodsky 2010). Therefore, using ShakeMaps based on observed and interpolated ground shaking seems to be a good possibility to improve the spatial aftershock estimation (section 2.1.1). However, ShakeMap data might be contaminated by site effects. Thus, if a rough geometry of the ruptured fault is known, using ground motion estimations based on ground motion models for hard rock (GMMs) may also be useful (section 2.1.2). In the case of known fault geometry it is also possible to use the empirical spatial ETAS kernel which is evaluated as a function of minimum distance to the rupture area instead of the epicenter location. If additionally also a slip model is available, Coulomb stress change (ΔCFS) can be calculated (section 2.1.4). This can be helpful, because ΔCFS values have been found to often correlate to aftershock distributions (King et al. 1994, Harris 1998). If no slip inversions are available, one can use random slip distributions for the Coulomb stress calculations based only on fault geometry (either inverted or based on fault plane solutions, section 2.1.6) and mainshock magnitude. The correct rupture geometry is the most important input for static stress change calculations and when using greatly simplified slip, calculated stress fields would only differ very close to the fault plane compared to the calculation based on a time–consuming slip inversion (Steacy et al. 2004).

In section 2.3, the value of those additional source information for improving spatial aftershock forecasts is systematically tested. The test is applied to three well–known aftershock sequences in California, namely the 1992 Landers, the 1999 Hector Mine and the 2004 Parkfield earthquake sequences, for which the results

are presented in section 2.4. Section 2.5 gives a discussion of the so far achieved results. Part of this work has already been published in Bach and Hainzl (2012).

Testing the extended ETAS models described in chapter 2.1 revealed that including Coulomb stress change maps to model the spatial distribution of direct aftershocks markedly improves aftershock forecasting. Still, the stress calculations contain large uncertainties, like non-unique slip inversions. This can result in a number of published slip models for the same event, which differ in geometry and slip distribution. Comparing the results of the extended ETAS models using Coulomb stress changes based on published or random slip models revealed that the difference is very small and in some cases the use of random slip might even be able to better forecast the aftershock distribution than by using published slip distributions.

In chapter 3, I compare nine published slip models to random slip models in order to address the information content of those inversions with respect to aftershock forecasting. The relative number of random models performing better than the published slip model is the quantity used to compare the performance of several published slip models. Detailed description of the used methods can be found in section 3.2. The aim is also to find similarities and differences in the published slip models which may explain good or bad performance in the tests. Though the influence on the results by randomly varying the slip distribution is investigated, as well as the influence of changing the fault geometry or slip patch (subfault) resolution. The results are given in section 3.4 and a discussion of the results is given in section 3.5. The overall findings and conclusions are given in chapter 4.

2 Improving empirical aftershock modeling based on additional source information

2.1 Model

The developed model approach focuses on improving the spatial forecast of those aftershocks directly triggered by the mainshock. For this purpose additional source information are used which are typically available for mainshocks. To do this in a robust way, the additional information are implemented within the framework of the Epidemic Type Aftershock Sequence (ETAS) model, which is one of the standard models for earthquake clustering and aftershock prediction. The ETAS model is a point process model for which earthquakes are characterized by their location-time-magnitude parameters (x, y, z, t, M). Introduced by Ogata (1988, 1998) it represents the seismicity as superposition of background and triggered events where every past event increases the probability of new events according to empirical relations for the magnitude-dependent productivity and the spatial and temporal aftershock distribution.

A representation of the temporal behavior of aftershock activity is provided by the Omori-Utsu formula (Utsu et al. 1995):

$$N(t) = \frac{K}{(t+c)^p} \tag{2.1}$$

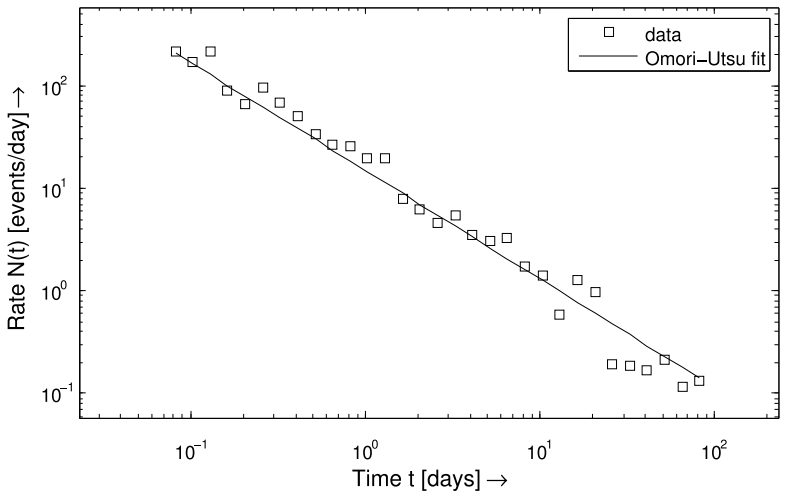

Figure 2.1: An example of temporal aftershock decay following the empirical Omori-Utsu law. The plotted sequence are $M >= 3$ aftershocks of the 1992 Landers (California) earthquake.

Here $N(t)$ is the occurrence rate of aftershocks per unit time with magnitudes greater than a lower cutoff M_{min}, where t is the elapsed time since the mainshock, K is a scaling parameter depending on the lower bound of the magnitude (M_{min}) of aftershocks being counted in $N(t)$. The parameter c is used because the function would diverge at $t = 0$ otherwise, however its value is strongly influenced by incomplete detection of small aftershocks at the beginning of the aftershock sequence. The exponent p is the slope of the aftershock decay rate in a log-log scaling and is usually between 0.9–1.5. The variability may be related to structural heterogeneities, stress, and temperature in the crust (Guo and Ogata 1997). An example of an aftershock sequence following an Omori-Utsu like temporal decay is shown in Figure 2.1. The plotted data are magnitude $M >= 3$ aftershocks of the 1992 Landers (California) earthquake selected using the criteria of Knopoff and Gardner (1974). The parameters used to plot the Omori-Utsu decay curve are taken from Woessner et al. (2011) ($c = 0.003$ and $p = 1.06$), who estimated them using the first 24 hours aftershock data.

The aftershock trigger potential scales exponentially with the earthquake magnitude, it is commonly described as being proportional to $\sim e^{\alpha(M-M_{min})}$ (Helmstetter

et al. 2005, Marsan and Lengliné 2008). The exact value of α varies strongly between different studies, in particular due to different optimization methods. A typical value would range around $\alpha = 1.84$ (Hainzl et al. 2013).

In the general case of having only earthquake catalog information (time, epicenter, magnitude) as input for the ETAS model, the spatial function is necessarily isotropic and is often modeled by a power law decay (Console et al. 2003, 2006, Hainzl et al. 2008)

$$f_i(\vec{x}) = f_{iso}(\vec{x} - \vec{x}_i) = \frac{(q-1)\, d^{2(q-1)}}{\pi[|\vec{x} - \vec{x}_i|^2 + d^2]^q} \ , \tag{2.2}$$

where d and q are two free parameters. The parameter q is usually around 1.5 which would be consistent with static stress triggering decaying according to $\sim r^{-3}$. A more general form accounting for anisotropy was originally proposed by Ogata (1988). However, the inversion of the additional used matrix S from earthquake data is not straightforward and must be estimated for each event independently, assuming an identity matrix the equation results in the here used isotropic version (Hainzl et al. 2008). In the following, this model using isotropic distance decay is called $ETAS_{\text{basic}}$.

The three empirical relations are used in the ETAS model to estimate the total occurrence rate of earthquakes according to

$$\lambda(t, \vec{x}) \ = \ \mu \ + \ \sum_{i:t_i<t} \frac{K e^{\alpha(M_i - M_{min})}}{(t - t_i + c)^p} f_i(\vec{x}) \ , \tag{2.3}$$

where μ is a constant background rate, modeled by a stationary Poisson process. For simplicity a uniform background rate is assumed because the estimation of space dependence requires rather arbitrary smoothing procedures of precursory seismicity. The difference to the use of space dependent background rates is expected to be small because the background rate is additive in the ETAS formulation and the considered time intervals are small. The second part of equation

Table 2.1: Different tested model combinations and their necessary input information for modeling the spatial aftershock distribution. For a detailed description of the individual models see Section 2.1.

Model	Used Mainshock Information				
	Epicenter	FPS	ShakeMap	Fault Geometry	Slipmodel
$ETAS_{\text{basic}}$	X				
$ETAS_{\Delta\text{FPS}}$	X	X			
$ETAS_{\text{ShakeMap}}$			X		
$ETAS_{\text{GMM}}$				X	
$ETAS_{\text{basic+fault}}$				X	
$ETAS_{\Delta\text{CFS (randomslip)}}$				X	
$ETAS_{\Delta\text{CFS}}$				X	X
$ETAS_{\Delta\text{CFS+ShakeMap}}$			X	X	X

2.3 takes account of the contributions of all previous events to the aftershock rate. Depending on the spatial and temporal distance and the magnitude, the events differently contribute to the expected rate.

Having additional external information about the spatial probability distribution of direct aftershocks, one can exchange the function $f_{iso}(\vec{x})$, which describes the spatial aftershock distribution using the empirical isotropic distance decay, for the specific mainshocks m by $f_m(\vec{x})$ containing the additional information. The functions $f_m(\vec{x})$ depend on the chosen model which are presented in the following subsections. Using this, the sum in equation 2.3 is splitted into two parts, the first accounting for all events without additional information, the second part accounting for all mainshocks for which additional information are available. With that the ETAS model becomes

$$\begin{aligned}\lambda(t,\vec{x}) \;=\; \mu \;+\; & \sum_{k:t_k<t} \frac{Ke^{\alpha(M_k-M_{min})}}{(t-t_k+c)^p} f_{iso}(|\vec{x}-\vec{x}_k|) \\ & + \sum_{m:t_m<t} \frac{Ke^{\alpha(M_m-M_{min})}}{(t-t_m+c)^p} f_m(\vec{x}) \;,\end{aligned} \tag{2.4}$$

where k denotes the index of the smaller magnitude events for which no additional source information are available.

The following subsections describe how the spatial probability distributions $f_m(\vec{x})$ can be calculated for direct aftershocks in the case of different input information and thus different assumptions about the underlying triggering mechanism. For a summary of all tested models with their necessary input information see Table 2.1.

2.1.1 ShakeMap Information: $ETAS_{\mathsf{ShakeMap}}$

ShakeMaps are usually one of the quickest information available, beside earthquake catalog data. They describe the extent and distribution of strong ground motion following large earthquakes worldwide. Shaking is caused by the passing of seismic waves, this is a dynamic effect limited in time and decreasing for larger distances. The effect of shaking is expected to be always positive, that means aftershocks are stimulated which is consistent with the ETAS formulation. The maps are constrained partly by measured ground motions and intensity data coupled with rupture dimensions resolved with rapid finite-fault analyses (Wald et al. 2008). In areas of sparse station coverage observations of peak ground acceleration (PGA) and peak ground velocity (PGV) are interpolated with the help of ground motion models (GMM). The shaking data might be contaminated by near surface effects, so called site effects, which might have strong influence on the shaking amplitude, e.g. due to amplification in sedimentary basins.

Because the peak dynamic strain can be assumed to be proportional to PGV, the intensity of triggered aftershocks is expected to be simply proportional to PGV in the case of dynamic stress triggering (van der Elst and Brodsky 2010). Thus, in this case $f_m(\vec{x}) = C^{-1} \cdot PGV(\vec{x})$ is used with C being the normalization constant determined by $C = \int PGV(\vec{x})d\vec{x}$.

2.1.2 Ground Motion Model: $ETAS_{GMM}$

Characterizing site conditions of ground shaking is not an easy task because of diverse geologic materials and irregular shaped earth structures. Peak ground velocity shows higher amplifications for soil sites than rock sites (Aki 1993). To avoid this one can also use ground motion models (GMM) as an alternative to ShakeMaps to estimate the peak ground velocity related to the mainshock. These maps are not produced using any direct measurements, as a result they cannot be contaminated by site effects. To estimate the distant dependent PGV, the knowledge of the rupture geometry for the calculations is necessary. Here the ground motion relation developed within the NGA-project by Campbell and Bozorgnia (2008) is used for the estimations. The probability map for the spatial aftershock distribution is obtained by normalizing the PGV values. Also this model is in general agreement with the ETAS approach, because shaking is assumed only to activate, not to deactivate.

2.1.3 Empirical Fault Distance Relation: $ETAS_{basic+fault}$

This extension is also using an empirical fault distance relation like GMM to describe the anisotropic spatial aftershock distribution. In this case, the distance decay is described using the ETAS kernel (equation 2.2), which involves two free parameters and the distance to the fault.

Like for the GMM, the decay is calculated using the minimum distance to the ruptured fault, this contrasts the basic ETAS model where the distance is always calculated relative to the epicenter. The two parameters d and q are assumed to be the same for the anisotropic and the isotropic case and set by fitting pre-mainshock events. It is important to explicitly normalize for the anisotropic case, while the function is already normalized in the isotropic case (equation 2.2).

2.1.4 Static Coulomb Failure Stress: $ETAS_{\Delta CFS}$

One more physical description of seismicity is based on the assumption that seismic events modify the stress field around the ruptured fault. There are studies putting in evidence that sudden stress variations can produce large variations of the seismicity rate (Console et al. 2006). The spatial patterns of Coulomb Failure Stress changes (ΔCFS) and aftershock distributions are often found to be correlated in a way that more aftershocks occur in areas of positive than in areas of negative stress changes (Harris 1998). In particular, best correlations of Coulomb stress change with aftershock distributions have been observed at distances greater than a few kilometers from the fault (King et al. 1994). On a fault plane of a given orientation, the Coulomb stress change is defined according to

$$\Delta CFS = \Delta\tau + \mu(\Delta\sigma_n + \Delta P) \ , \tag{2.5}$$

where $\Delta\tau$ is the shear stress change in slip direction, $\Delta\sigma_n$ the normal stress change, ΔP the pore pressure change and μ the coefficient of friction (Harris 1998). A positive stress change indicates an increased tendency that the fault will slip in direction of interest, whereas a negative stress change indicates a reduced tendency to slip.

Figure 2.2 illustrates equation 2.5 in a graphical way and shows the spatial distribution of right–lateral shear stress change, normal stress change and right–lateral Coulomb stress change resolved on faults parallel to the master fault. The calculations are based on a vertical north–south oriented fault with dimension 40 km x 15 km. The slip distribution is uniform and the amount of slip corresponds to an event with magnitude 6. Stress calculations are based on the formulations of Okada (1992). Highest stress changes occur very close to the fault, the distance decay is proportional to r^{-3} in the far field. At the margins of fault patches, the calculated stress field has singularities. To reduce the influence of excessively high stress change values in models based on the stress field, a common method is to

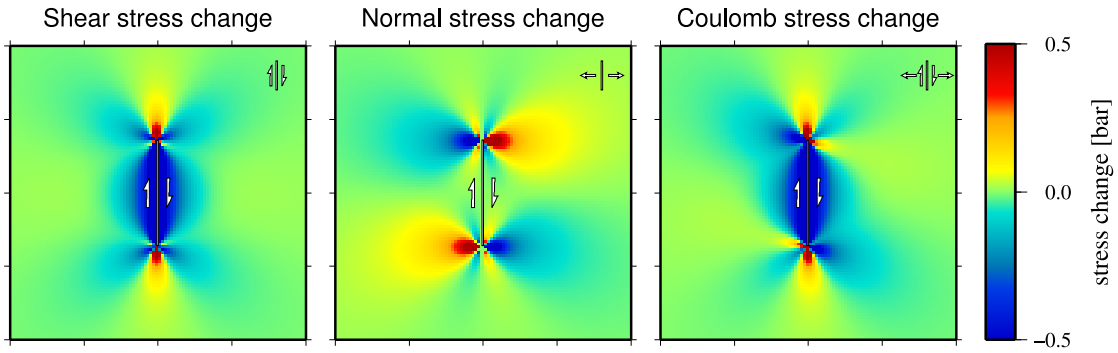

Figure 2.2: This illustration shows a graphical representation of equation 2.5. The stress calculations are based on a vertical north–south oriented strike–slip fault embedded in an elastic half–space. The slip distribution is uniform. The stress change is resolved on right–lateral faults parallel to the master fault. The map size is 1° x 1°, the fault size is 40 km x 15 km. The uniform slip corresponds to an event of magnitude 6.0.

cut off the stress values at a predefined maximum stress change.

Static stress triggering has been questioned because correlations between calculated stress and aftershock activity are typically not very high (Hardebeck et al. 1998) and aftershocks occur also in stress shadows where the model predicts a decrease in seismicity rate (Marsan 2003). Recently, it has been shown that this apparent contradiction can be resolved by taking the involved small-scale slip variability and the large uncertainties of stress calculations into account (Marsan 2006, Hainzl et al. 2009). In general, the calculation of Coulomb stress changes involves large uncertainties because of (1) the non uniqueness of slip inversions, (2) the unknown receiver fault mechanisms, (3) undetectable small-scale variations of slip and fault geometry, which can lead to strong stress heterogeneities close to the source fault, and (4) spatial inhomogeneity of material and prestress conditions (Hainzl et al. 2009).

Coulomb stress calculations require a slip distribution of the earthquake rupture process and the definition of the receiver faults on which stress perturbations are resolved. The published slip models used in the first part of this work are shown in Table 2.2. Additionally, the use of random slip models is tested because

Table 2.2: Information related to the slip models and standard deviations used for Coulomb stress calculations. Strike and dip values are chosen according to the average mainshock mechanism, rake value according to the general tectonic regime in California.

	1992 Landers	1999 Hector Mine	2004 Parkfield
Magnitude	7.3	7.1	6.0
Slip Model	Wald and Heaton (1994)	Ji et al. (2002b)	Custódio et al. (2005)
Depth Layers	3–13 km	3–13 km	3–13 km
Receiver Fault Strike	$330° \pm 20°$	$335° \pm 20°$	$140° \pm 20°$
Receiver Fault Dip	$90° \pm 20°$	$80° \pm 20°$	$87° \pm 20°$
Receiver Fault Rake	$-180° \pm 20°$	$-180° \pm 20°$	$-180° \pm 20°$

reliable slip inversions are usually not available very quickly. In this case, each slip model is constrained by fault geometry and earthquake magnitude, the spatial probability distribution results from averaging the calculated probability maps of many random slip realizations. The random slip is tapered towards the margin and high frequencies are damped using a k^{-2} slope, k is the radial wave number (Herrero and Bernard 1994).

Using equation 2.5, the stress change is calculated for specific receiver fault orientations. Two concepts are commonly used to select the receiver mechanisms. Either one manually fixes a predefined fault orientation or uses optimal oriented fault planes where the Coulomb stress change is locally maximum. Often it is assumed, that aftershock fault planes are optimally oriented, that means the regional stress and coseismic stress is resolved onto these orientations. Both cases are not very realistic because choosing the relevant fault plane involves uncertainties and the seismogenic crust is typically fractured in a complex way. Thus, in nature receiver faults will have a number of different orientations, often consistent with mapped structural trends, on which earthquakes are able to nucleate (Steacy et al. 2005). An example Coulomb stress change map based on the Wald and Heaton

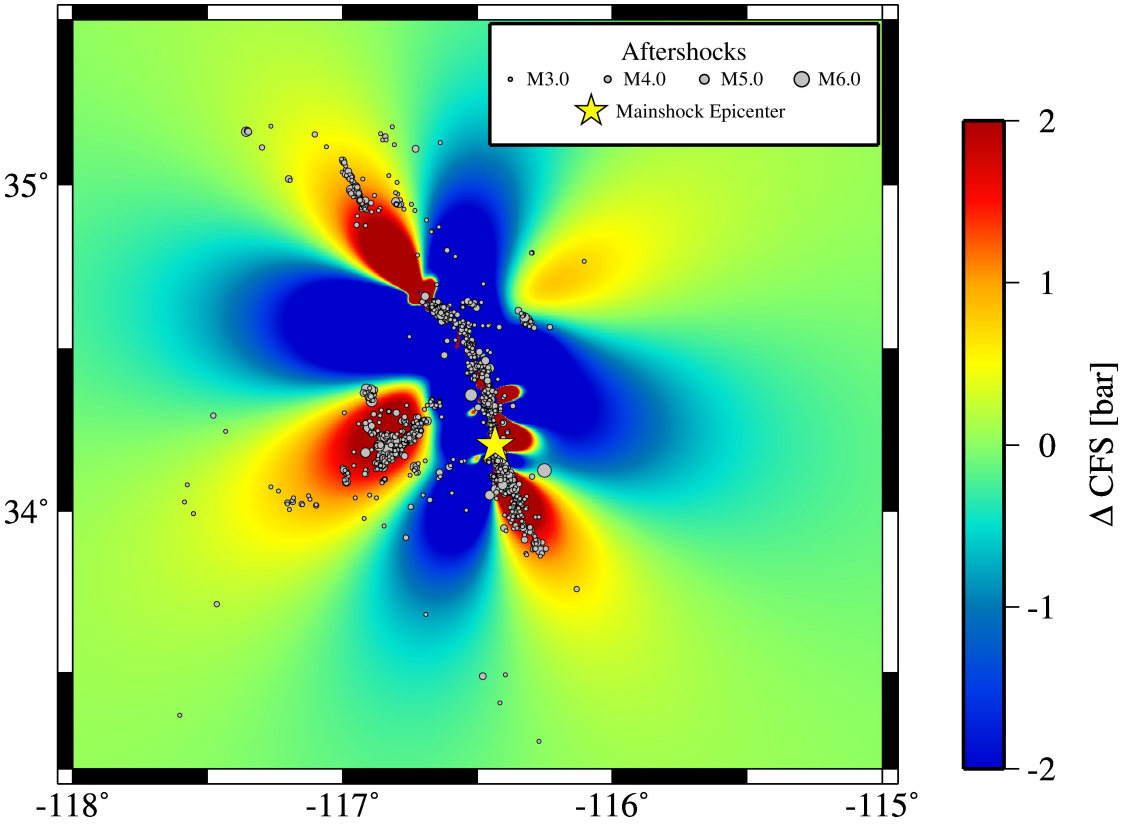

Figure 2.3: This plot shows the Coulomb stress change in a depth of 7 km for the Landers 1992 mainshock. The calculations are based on the Wald and Heaton (1994) slipmodel, using fixed receiver planes with strike = 330°, dip = 90°, rake = −180°. Gray dots represent one year $M >= 3$ aftershocks, dot size scales with magnitude, the yellow star indicates the epicenter of the mainshock.

(1994) slip model is shown in Figure 2.3. The aftershocks, represented by gray dots, fairly well follow the stress change pattern, especially more distant to the fault most of the aftershocks occurred in areas of positive stress change. However, the stress pattern close to the ruptured fault is much more irregular, the stress orientation changes frequently for small distances. This might be due to unresolved small scale slip variations which can not be detected.

Uncertainties are taken into account by using variations of receiver fault orientations, and by calculating the Coulomb stress change at several depth layers. In the following applications, the average mechanism of the aftershocks is assumed to

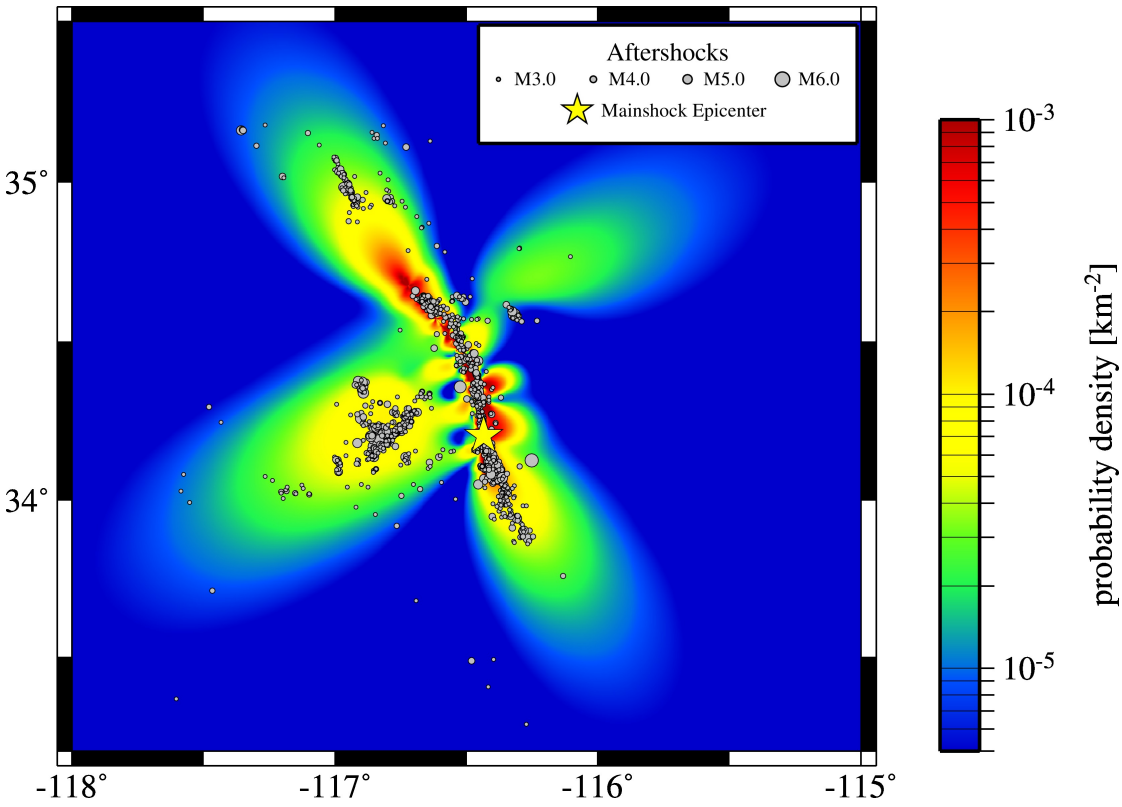

Figure 2.4: This plot shows a Coulomb stress change based aftershock probability map. The calculations are based on the Wald and Heaton (1994) slipmodel, receiver fault mechanisms are randomly selected using the mean mainshock mechanism and a Gaussian distribution with $\delta = 20°$. Gray dots represent one year $M >= 3$ aftershocks, dot size scales with magnitude, the yellow star indicates the epicenter of the mainshock.

be identical to that of the mainshock. Next, the stress changes for a large number of receiver mechanisms is calculated, these are taken randomly from a Gaussian distribution of strike, dip and rake values according to (Hainzl, Zöller and Wang 2010). Here it is assumed, that the distributions of aftershock mechanisms are homogeneous in space.

A clock advance model introduced by Hainzl, Brietzke and Zöller (2010) is utilized to translate the calculated stress changes into an aftershock probability map. Based on basic assumptions, this model yields the general prediction that the number of aftershocks is directly proportional to ΔCFS in the case of positive stress

changes while no aftershocks are expected in regions of negative stress changes. For N randomly selected aftershock mechanisms and Z depth layers, the aftershock probability map according to this model is given by

$$f_m(\vec{x}) = C^{-1} \sum_{k=1}^{Z} \sum_{i=1}^{N} \Delta CFS_{ik}(\vec{x}) H(\Delta CFS_{ik}(\vec{x})) \ , \tag{2.6}$$

where H denotes the Heaviside function ($H(s) = 1$ for $s \geq 0$ and 0 else), indexes k and i are counters for the aftershock mechanism and depth layer. Here, the constant C is again given by normalization, that means by the constraint that $\int f_m(\vec{x}) d\vec{x} = 1$.

The probability map for the Landers mainshock corresponding to the stress change shown in Figure 2.3 is shown in Figure 2.4. By considering many possible receiver fault mechanisms, the small scale stress changes close to the fault diminish. Now the aftershock distribution near the fault much better fits areas of high probability density.

The static stress triggering model is in general not consistent with the ETAS model because of the prediction of areas with suppressed activity (relative to the background rates) while the ETAS model only accounts for activation. This is less problematic because the number of missing events due to negative stress changes will be very small on the short timescales considered here. Furthermore, regions of seismic quiescence will vanish if the uncertainties are considered in the stress calculations (Hainzl, Zöller and Wang 2010). The same applies in this case, where the calculated aftershock rate is in almost all locations significantly larger than the background rate. Thus also the addition of the constant background rate in the ETAS model will not affect the results notably.

2.1.5 Combining Static and Dynamic Stress Changes: *ETAS*$_{\Delta\text{CFS+ShakeMap}}$

In reality, static and dynamic stress triggering might act simultaneously. According to the analysis of van der Elst and Brodsky (2010), dynamic stress changes are responsible for approximately 50% of the aftershock generation. To account for this, one model is tested in which both ShakeMap and ΔCFS probability maps are combined with equal weights.

2.1.6 Fault Plane Solutions: *ETAS*$_{FPS}$

The availability of the geometry of the ruptured fault for Coulomb stress calculations is not always given. In that case fault plane solutions might help as they give the two possible nodal planes of the rupture. Here, that plane is selected from the global CMT catalog, which agrees with the general fault regime in that area (NW–SE in California). The dimension and displacement of the fault can be calculated using empirical relations like that of Wells and Coppersmith (1994). They compiled a worldwide data base of source parameters for 421 historical earthquakes. Different relations are given depending on the slip type.

As patch resolution a size of approximately 2x2km has been chosen, this is in the same range of many published slip models. The average slip is based on the relations of Wells and Coppersmith (1994), whereas the slip distribution is chosen to be random, like described in section 2.1.4. The location of the fault is taken from the CMT catalog, which gives the center of the earthquake moment distribution. Consequently this location is used as central point for the estimated fault plane. Details about the fault plane solution used for the tested events are given in Table 2.3.

2.2 Data

The hybrid models described in chapter 2.1 are tested for three different Californian earthquakes and their aftershock sequences. In particular, these are the 1992 M7.3 Landers, the 1999 M7.1 Hector Mine and the 2004 M6.0 Parkfield earthquake. On the one hand this allows a comparison of the models performances for different target areas and magnitudes, on the other hand one should remember that these three earthquakes occur in a very similar tectonic environment and results might be different in another tectonic setting. So before using the models in other regions one should retrospectively test their performance for the specific area.

2.2.1 Aftershock catalog and parameter inversion

The spatial area for the tests is chosen according to the coverage of the ShakeMap. The parameter optimization is done only for events which occurred before the mainshock, this accounts for a more realistic test, where no aftershock data were available yet. The temporal window for the optimization should be as long as possible to achieve stable results, here, a period of 10 years is used and the same spatial window as for the tests. 365 days of aftershocks are used as testing period for all models. For all sequences we use the relocated catalog by Hauksson et al. (2012) to get precise epicenter information. This catalog contains events in Southern California from 1981 to June 2011. Locations are very precise, 90% of the absolute horizontal errors are less than 0.75 km and 90% of the vertical errors are less than 1.25 km. The relative errors that were determined are one order of magnitude smaller than the absolute errors.

For the purposes of this work, the catalog is filtered according to the investigated spatial area and time window, and a minimum magnitude M_{cut} of 3.0. The Landers sequence contains 2096 events, 1411 are aftershocks, though 685 events occurred in this area during 10 years period before the mainshock. The Hector Mine sequence contains 3447 events matching the magnitude, time and space conditions, where

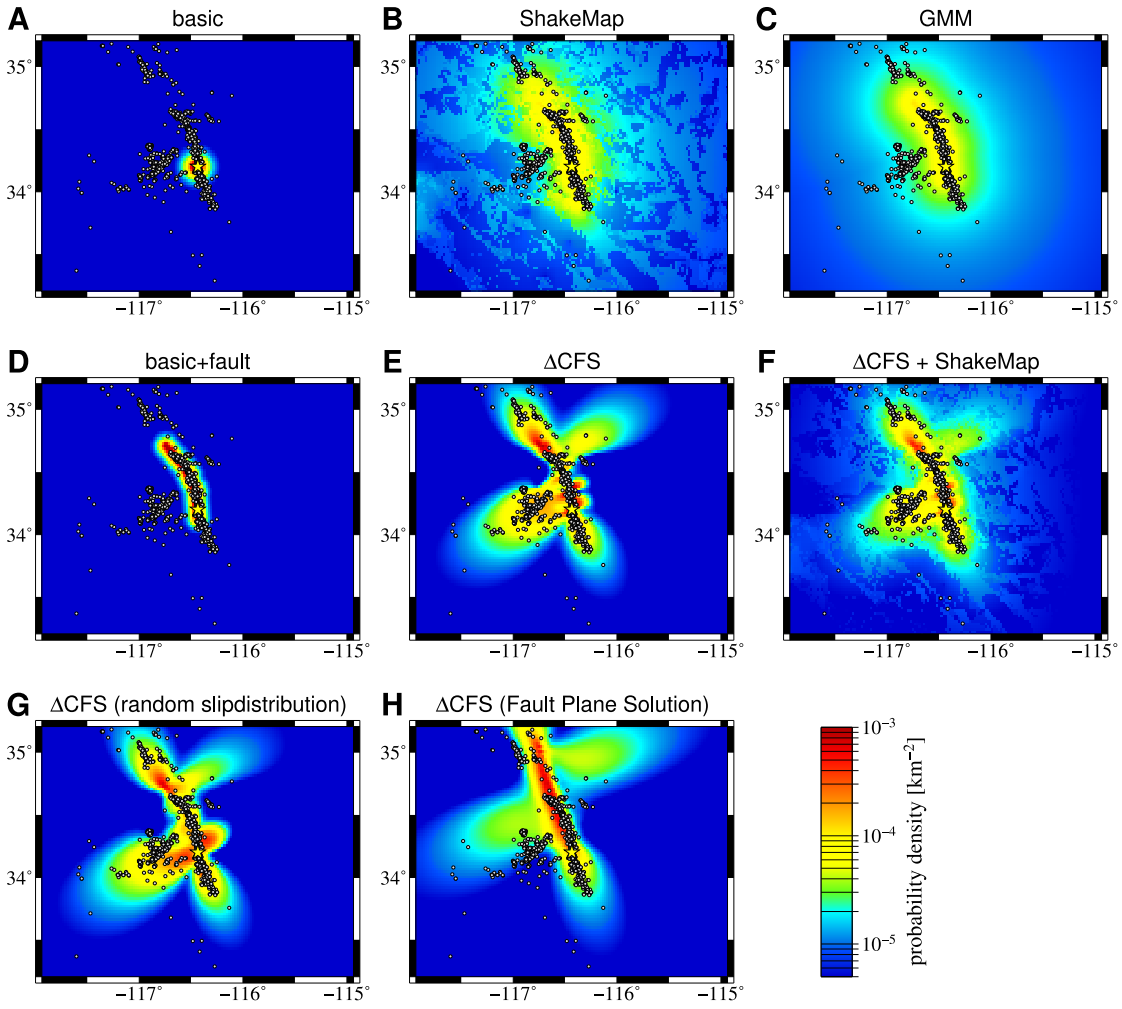

Figure 2.5: Calculated probability maps for the Landers earthquake. **A**: probability map used in the basic ETAS model, **B**–**H**: probability maps based on ShakeMap, GMM, the ETAS spatial kernel applied to the nearest distance to the ruptured fault, ΔCFS, a combination of ΔCFS and ShakeMap data and ΔCFS based on random slip distributions using the published fault geometry or a fault plane solution based geometry. Gray dots represent the epicenters of the $M \geq 3$ aftershocks within the first 365 days and the yellow star indicates the mainshock epicenter.

671 events are aftershocks and 2776 occurred before the mainshock. The Parkfield sequence contains 291 events with 236 foreshocks and 55 aftershocks.

Fault plane solutions used to estimate the rupture geometry are taken from the global CMT catalog. This is available at `www.globalcmt.org` (last access June

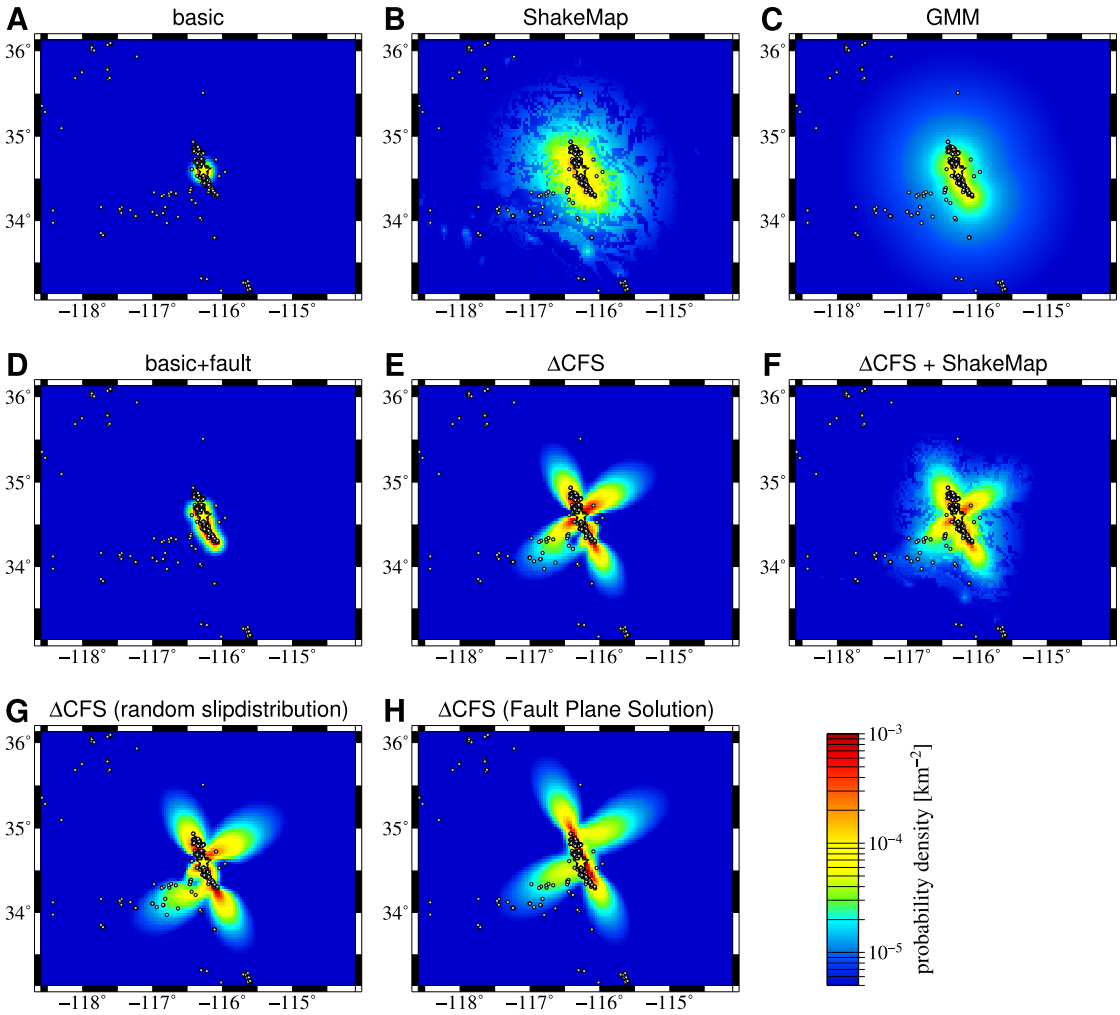

Figure 2.6: (A–H) Calculated probability maps for the Hector Mine earthquake (see Figure 2.5 for detailed description).

2013). The global CMT project started approximately 30 years ago in order to create a consistent catalog of earthquake mechanisms. More details about the project can be found in the publications of Dziewonski et al. (1981) and Ekström et al. (2012). The fault plane solutions used for this study are given in Table 2.3.

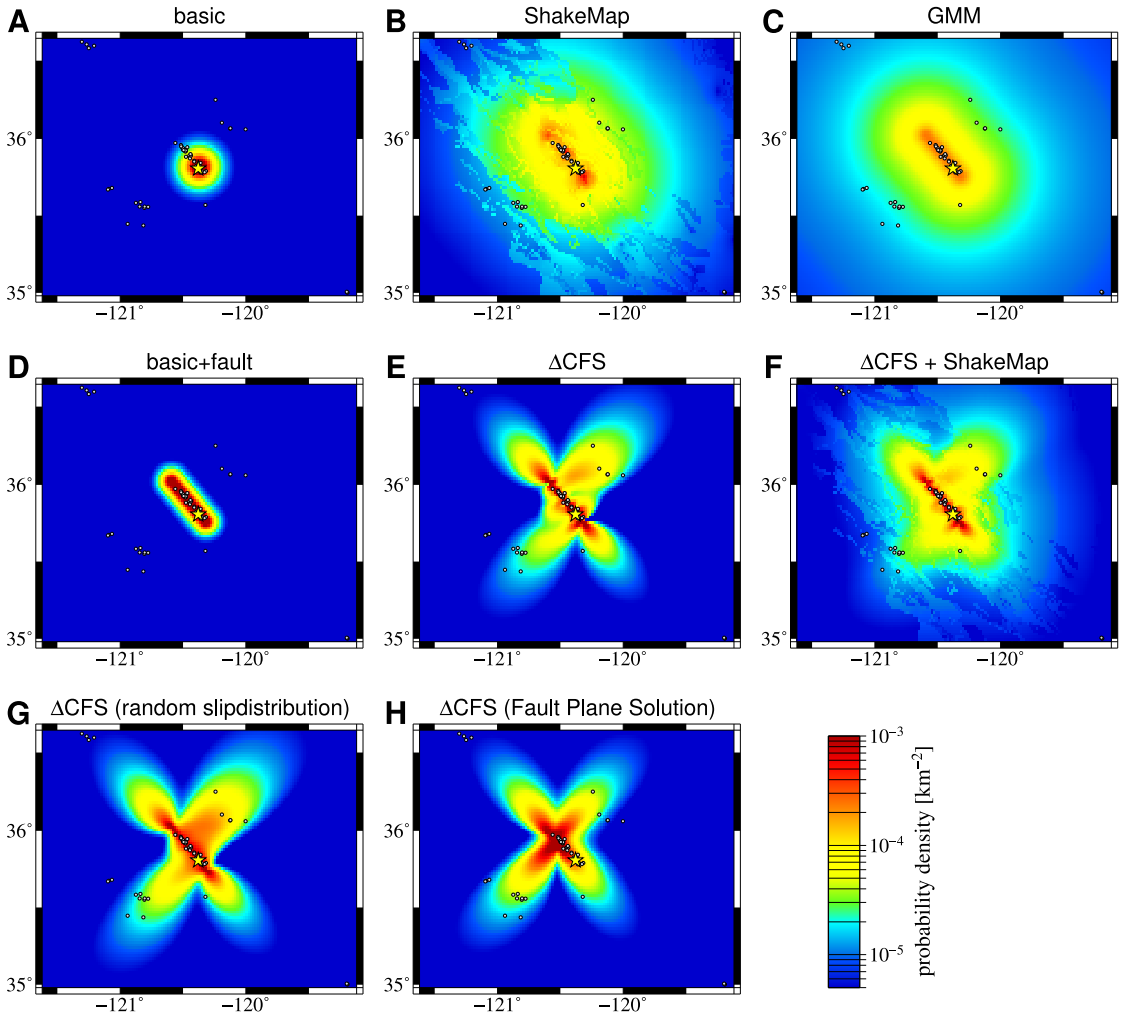

Figure 2.7: (A–H) Calculated probability maps for the Parkfield earthquake (see Figure 2.5 for detailed description).

2.2.2 Spatial probability maps

For the Coulomb stress calculations the software of Wang et al. (2006) for layered half-space is used. In each case, the same 1D velocity model is used as for the slip inversions. The slip models are taken from the finite-source rupture model database maintained by Martin Mai (see http://seismo.ethz.ch/static/srcmod/). The ΔCFS calculations are done using a horizontal spatial grid with spacing of $\sim$ 2 km, this limitation is necessary to limit the calculation time. For all other

Table 2.3: Fault plane solutions from global CMT catalog used to estimate the rupture geometry of the Landers, Hector Mine and Parkfield earthquake. Fault size and average slip estimations are based on Wells and Coppersmith (1994).

	1992 Landers	1999 Hector Mine	2004 Parkfield
Magnitude	7.3	7.1	6.0
Center (lat, lon)	$(34.65°, -116.65°)$	$(34.71°, -116.27°)$	$(35.92°, -120.54°)$
Strike/Dip/Rake	$341°/70°/-172°$	$336°/80°/174°$	$321°/72°/-178°$
Fault Size	90x16km	68x14.3km	14.1x7.2km
Average Slip	1.8m	1.2m	0.12m

model extensions, the same horizontal grid resolution is used. For the calculations, $N = 100$ aftershock mechanisms and $Z = 11$ depth layers between 3 and 13 km with a spacing of 1 km are randomly selected. Generally, the faults in southern California have NW–SE orientations, and are almost entirely vertical strike-slip (McCloskey 2003). Here, it is assumed that the mean strike and dip is in agreement with the mainshock mechanism, while the rake was set to $-180°$ in agreement with the right lateral strike-slip regime in California. Additionally, a normal distribution with a standard deviation of $\pm 20°$ for strike, dip and rake values of the aftershock mechanisms is assumed according to Hainzl, Zöller and Wang (2010). All information about the Coulomb stress calculations are summarized in Table 2.2 and 2.3.

The calculated probability maps and the aftershock distribution for the three investigated sequences are shown in Figures 2.5, 2.6 and 2.7. The aftershock distribution is clearly anisotropic, it is elongated in NE–SW direction, which is in agreement with the general fault orientations in California and clusters around the fault traces of the mainshock. Modeling the aftershocks of large events by an isotropic distribution, as done in the basic ETAS model (also see Figures 2.5A, 2.6A and 2.7A), obviously leads to wrong forecasts. The probability maps derived from ShakeMap data and the GMM calculation are in general very similar, just

the GMM calculations lead to smother results. The map resulting from the ETAS spatial kernel evaluated relative to the minimum distance to the fault segment is also similar, however, it predicts a much stronger decay with distance than the forecasts based on the ground motion data. Figure 2.8 emphasizes this difference, which leads to higher probability density close to the fault for the $ETAS_{\mathrm{basic+fault}}$ model compared to the $ETAS_{\mathrm{GMM}}$ model, and lower probability density at larger distances, respectively. Completely different to the other distributions is the probability map based on static Coulomb stress change, this one is much more irregular (Figures 2.5E, 2.6E and 2.7E). It has large lobes of higher probability density pointing away from the fault trace. The maps based on Coulomb stress changes using random slip distributions and the ones based on fault plane solutions are in general very similar to the one using the published slip model. The largest differences are visible in Figure 2.5H, the fault plane solution based stress change map for Landers. Areas of high probability density extend much more to the north, because the fault plane consists only of one segment, extending 45 km to NNW and 45 km to SSE from the central point of earthquake moment release. The published slip model has approximately the same length in total, but the three segments slightly overlap and are curved towards the west.

Although the visual comparison with the observed aftershocks can already give some hints about the forecasting ability of each model, it is necessary to perform a quantitative test. This is particularly important because the probability maps only describe the spatial distribution of directly triggered aftershocks, while observed seismicity also includes background as well as secondary aftershock activity. In Figure 2.5 this becomes very obvious, the cluster in the West (-116.8°W, 34.2°N) is mainly related to secondary aftershocks triggered by the M6.4 Big Bear event, the largest aftershock in the Landers 1992 sequence. In the ETAS model approach, this secondary cluster will be mainly attributed to the isotropic aftershock distribution of the Big Bear event and not to the Landers mainshock. In the next sections the results for a comprehensive, comparative test of the different models is described.

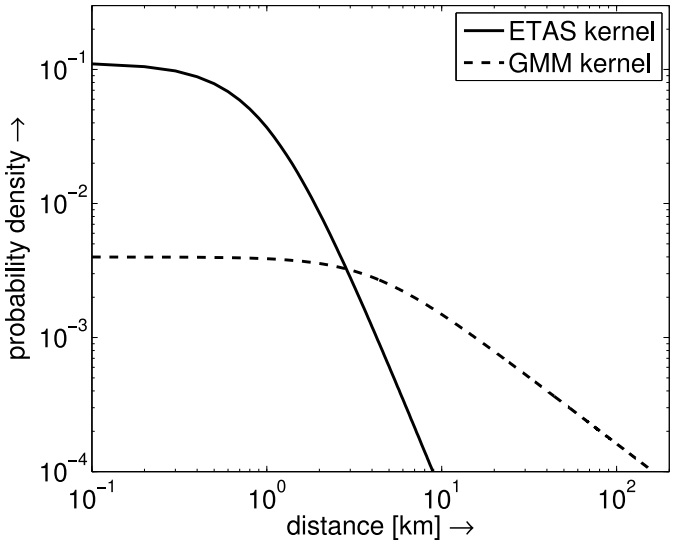

Figure 2.8: Comparison of the decay of the ETAS and the GMM kernel which are used for the $ETAS_{\text{basic+fault}}$ and the $ETAS_{\text{GMM}}$ model, respectively.

2.3 Model Application

In this section the extensions of the ETAS model using the different information related to the mainshocks are discussed. The earthquake model is described by equation 2.4 where $f_m(\vec{x})$ is replaced by the different probability maps derived from the different additional inputs, displayed in Figure 2.5 for the example of the Landers mainshock.

2.3.1 Inverting for the ETAS parameters

The first step in the model testing process is the estimation of the ETAS parameters $\theta = (\mu, K, c, \alpha, p, q, d)$. Either they are already known for that region or they have to be optimized using the seismicity in the region of interest. To construct the tests more realistic, the optimization in this work is done using only events which occurred before the mainshock. Consequently the resulting ETAS parameters used for all model applications are the same for one specific earthquake sequence. The parameters θ are calculated for all $M \geq 3$ events for a time period of 10 years

before the mainshock by maximizing the logarithmic likelihood function.

The likelihood function

$$f(t_i, x_i, y_i) \;=\; \{\prod_{i}^{N} \lambda(t_i, x_i, y_i)\} \cdot exp\{-\int_{S}^{T}\iint_{A} \lambda(t, x, y) dx dy dt\} \;, \tag{2.7}$$

is derived by multiplying the probabilities of no events in the gaps $(t_{i-1}, t_i) \times (x_{i-1}, x_i) \times (y_{i-1}, y_i)$ between observed events and the probabilities $\lambda(t_i, x_i, y_i)\mathrm{d}t\mathrm{d}x\mathrm{d}y$ of events in the infinitesimal intervals $(t_i, t_i + \mathrm{d}t) \times (x_i, x_i + \mathrm{d}x) \times (y_i, y_i + \mathrm{d}y)$. The multiplication is possible due to the basic assumption of a Poisson process that the occurrences of events in separated intervals are independent. Consequently the logarithmic likelihood as given by Ogata (1983) is

$$lnL \;=\; \sum_{i=1}^{N} ln\lambda(t_i, x_i, y_i) - \int_{S}^{T}\iint_{A} \lambda(t, x, y) dx dy dt \;, \tag{2.8}$$

where t_i are the occurrence times of the N events with $M \geq M_{min}$ which occurred in the testing period $[S, T]$ and test region A. For the inversion process, $M_{min} = 3$, $S = -3650$ days and $T = 0$ days.

For this parameter inversion process the method of Davidon–Fletcher–Powell is utilized. This is a Quasi–Newton method for locating a local minimum of a function in $\mathbb{R}^n$. The maximization is performed numerically by using the gradients. The resulting parameter values and standard deviations for each of the three earthquake sequences are given together with the specifications of the space window in Table 2.4. The standard errors of the estimated parameters were calculated from the Hessian matrix. Some α values are quite low, probably because of the assumption of spatial isotropy of the earthquakes in the ETAS model during the optimization (Hainzl et al. 2008). To make sure that this does not influence the results, the models were also tested using a fixed value of $\alpha = 1.84$ and inverting only for the other parameters.

The ETAS parameters θ were then fixed for all models and used for the evalu-

Table 2.4: ETAS parameters and standard deviations calculated for the three earthquake sequences using 10 years of $M \geq 3$ pre-mainshock events. The parameters are constant in the forecast interval for all models.

	Landers	Hector Mine	Parkfield
latitude	[33.2, 35.2]	[33.1, 36.1]	[35.0, 36.6]
longitude	[-117.9, -114.9]	[-118.6, -114.1]	[-121.6, -119.1]
μ [days^{-1}]	0.044 ±0.004	0.052 ±0.005	0.008 ±0.002
K	0.03 ±0.003	0.047 ±0.002	0.030 ±0.005
c [days]	0.001 ±0.0003	0.0005 ±0.0008	0.008 ±0.007
α	1.21 ±0.099	0.83 ±0.038	1.17 ±0.104
p	0.95 ±0.016	1.06 ±0.008	0.84 ±0.030
q	1.40 ±0.033	1.40 ±0.014	1.57 ±0.093
d [km]	0.37 ±0.037	0.36 ±0.016	2.01 ±0.383

ation of the forecast ability of the $M \geq 3$ aftershocks which followed during the first 365 days after the mainshock. For simplicity, time is given in the following always in days relative to the mainshock occurrence time. Thus the optimization interval is [-3650, 0] days and the testing period is $[0, 365]$ days. In each case the investigated area was chosen according to the coverage of the ShakeMap and the grid size was limited to ~ 2 km due to rapidly increasing calculation times of the Coulomb stress changes.

2.3.2 Test setups

Two different test setups are performed. The first one is a forecast test (Test-A), in this case earthquakes which occurred before the mainshock are allowed to influence the aftershock probability, whereas observed aftershocks were not used to alter the forecasts. This test reflects the case where forecasts have to be given directly after the occurrence of the mainshock without any knowledge of aftershock

activity. The second test (Test-B) takes secondary triggering into account by using the information of the aftershock catalog. Thus the consistency of the full model with the observations is quantified. The forecasted earthquake rate $\lambda(t, \vec{x})$ at a given time t in the test period, is given in Test-A by equation 2.4 where the second sum is limited to $t_k < 0$ while the sum is evaluated for $t_k \leq t$ in the second test.

The test quantity in both cases is the logarithmic likelihood value of the models for the testing period (equation 2.8). In the standard case, $M_{min} = 3$, $S = 0$ and $T = 365$ days, while results for other values are discussed later. For easily comparing the different hybrid models, the average probability gain per event $e^{\Delta lnL/N}$ has been calculated. Here, $\Delta lnL = lnL_{model} - lnL_{ETAS_{basic}}$ is determined relative to the basic ETAS model, which facilitates the comparison of the different models and quantifies the improvement concerning the standard model. An information gain larger than one means, that the aftershock forecast is improved compared to the basic ETAS model, while values below one stand for a worsening.

Although most of the aftershock activity usually occurs close to the ruptured fault, future larger events might be expected to occur at more distant places, in particular at neighboring fault segments or larger hidden faults. To take care of both cases, the tests are performed for two different target events. On the one hand, the log likelihood is calculated for all aftershocks in the investigated area. In that case, the information gain is only related to the spatial forecast because all other model components are identical in the different models. On the other hand, the calculations are done only using aftershocks which occurred more than 5 km away from the ruptured fault in order to compare the ability of forecasting off-fault activity. Note that this test includes not only spatial information but also total rate information because the models forecast different numbers of events in the tested off-fault region.

To evaluate the robustness of the models, all tests were repeated for different cut-off magnitudes and different time windows. Also the use of fixed higher α values was tested, because the estimated values, especially for the Hector Mine sequence

(see Table 2.4), are quite low. Parameter uncertainties are propagated through the model by a Monte–Carlo selection of the logarithmic likelihood for 1000 model setups where the parameters were selected randomly from a normal distribution with mean and standard deviations displayed in Table 2.4. All parameters are allowed to vary at the same time. Note that the estimated standard errors of the resulting information gain may be overestimated, because parameter correlations are not considered.

2.4 Results

The test procedure was applied to the three earthquake sequences described in section 2.2. The resulting probability gain for the two tests and the two different target events is displayed in Figures 2.9 and 2.10.

2.4.1 Test-A

If all aftershocks in the first 365 days following the mainshock are taken into account (Figure 2.9A), the use of ShakeMap or GMM data is able to improve the aftershock forecasts for Landers and slightly for Hector Mine. For the Parkfield sequence, both more complex models taking dynamic stress triggering into account perform even a bit worse than the basic ETAS model. The reason might be the weak decay of PGV values with distance to the fault, which can not explain the large number of aftershocks very close to the fault. In contrast, the ETAS decay function resulting from the fit of precursory seismicity decays much faster with distance. The model using this seismicity based function evaluated as a function of minimum distance to the fault rupture (model $ETAS_{\mathrm{basic+fault}}$) results in a constantly large improvement for all earthquake sequences. This model performs best for the Hector Mine and Parkfield sequence. The results show that the use of Coulomb stress change maps improves the forecast ability best for the Landers sequence and second best for the other two sequences. The difference in using published or random slip models is mostly small. If the fault geometry used for the stress calculations is based on a fault plane solution, the model performance is worse compared to the other stress change based models, but still better than the purely statistical model $ETAS_{\mathrm{basic}}$. Anyway, the comparison with the ground–motion based forecasts reveals that the static stress triggering models always outperform the dynamic stress triggering models. Combining the static and dynamic stress information is not able to improve the models performances any more. Also using different weights of static and dynamic stress changes for the

combined model did not change the results much.

Figure 2.10A shows the probability gain only obtained using aftershocks more than 5 km away from the rupture area. It is found that the more distant aftershocks are best modeled using Coulomb stress change information. This is in agreement with findings of other authors (e.g. King et al. (1994)), who also find the best correlations of Coulomb stress change patterns and the aftershock distribution several kilometers away from the ruptured fault. The reason might be, that stress calculations more distant to the fault are less effected by small–scale slip variabilities which are not resolvable by inversions of observational data. Only for the Parkfield sequence the performance using static stress change or ShakeMap data is nearly the same. Contrasting the results of the test for all aftershocks,the model $ETAS_{\text{basic+fault}}$ shows the worst performance, for the Landers and Parkfield sequence it performs even worse than the basic ETAS model. The bad performance compared to the ShakeMap based model indicates that off-fault aftershocks are decaying slower with distance than the more frequent aftershocks in the vicinity of the fault. Figure 2.11 illustrates very well, that this model cannot be able to explain the more distant aftershocks. Within a few kilometers from the fault, the probability density decreases by several magnitudes, mostly not being able to explain the distribution of the 868 aftershocks (out of 1411), which occurred more than 5km away from the fault.

2.4.2 Test-B

Results for this test are presented in Figures 2.9B and 2.10B. For this test aftershock interactions are taken into account, that means every event is related to all previous events, not only to pre–mainshock events. This improved the $ETAS_{\text{basic}}$ model, so the probability gain for all extended models is smaller than in Test-A. The resulting probability gains reveal that the ETAS model is, except of small improvements for the Landers sequence, not able to benefit from the use of ShakeMap or GMM data. The $ETAS_{\text{basic+fault}}$ has the best results in this test, it outperforms

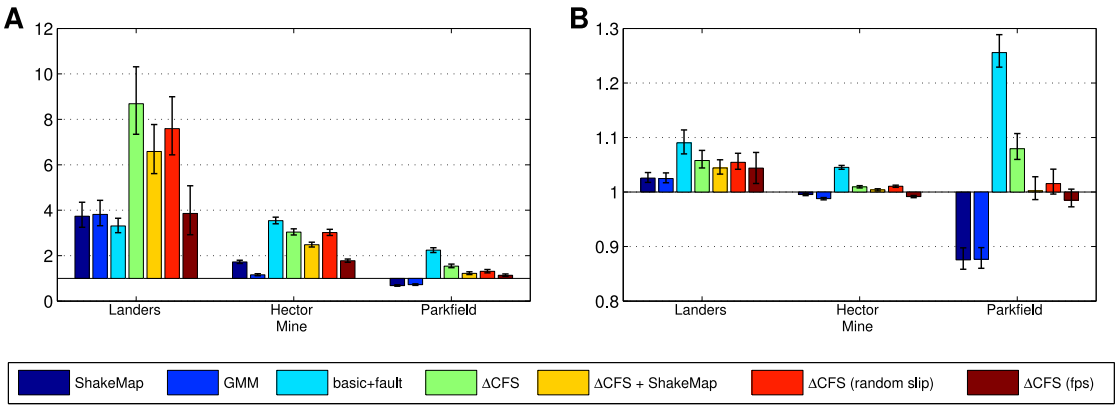

Figure 2.9: Probability gain for different models accounting for all events in the target region independent of their distance to the fault: (A) Results of Test-A and (B) the corresponding results for the Test-B. Error bars define the 68.3% confidence interval for 1000 simulations with randomly chosen ETAS parameters (see description in Section 2.3).

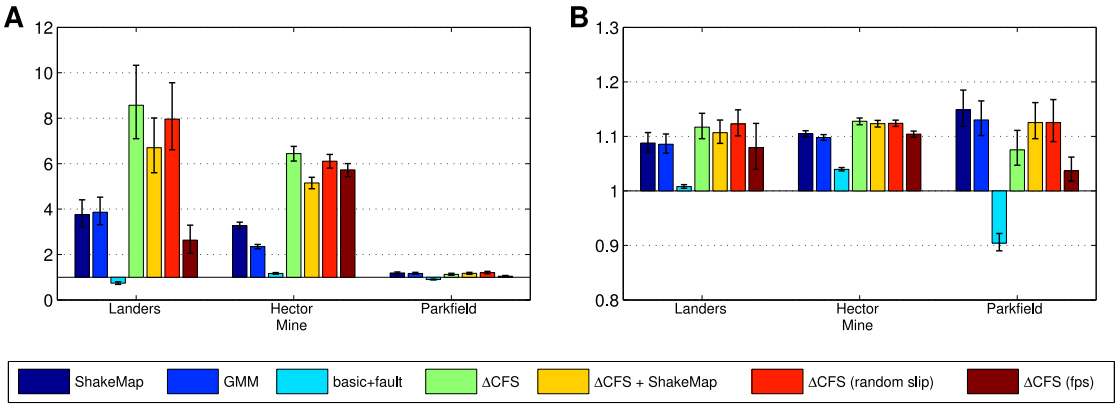

Figure 2.10: Probability gain for different models, same as Figure 2.9, but accounting for off-fault ($r \geq 5$ km) events only.

all other models for the three investigated aftershock sequences. The inclusion of Coulomb stress change maps improved the model, too. The same test excluding events closer than 5 km to the fault leads to similar results like for Test-A. The $ETAS_{\text{basic+fault}}$ model performs worse, whereas good results are obtained using Coulomb stress change or ShakeMap data. Furthermore, it is interesting to note that in some cases the information gain using random slip distributions is even slightly better than using the published ones. This will be further investi-

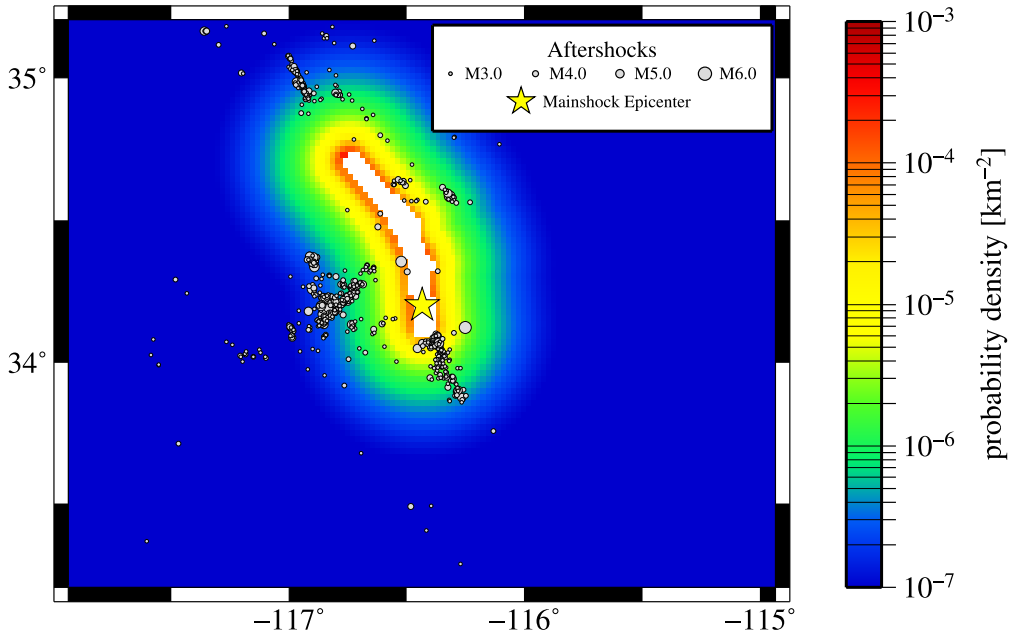

Figure 2.11: On this figure the probability density distribution of the $ETAS_{\text{basic+fault}}$ model and the aftershocks which occurred more than 5km away from the fault are plotted. White area is less than 5 km away from the fault. Note the changed color scale compared to previous plots.

gated in chapter 3 by comparing the performance of published slip models to the performance of a number of random slip distributions.

2.4.3 Seismic Hazard Analysis

For engineers and decision makers it is essential to know about the seismic risk, either to create building codes or decide about evacuation time and area due to aftershock risk following large earthquakes. Probabilistic seismic hazard analysis (PSHA) is the attempt to quantify seismic risk in terms of ground shaking due to earthquakes at a specific site and for the time period of interest (Cornell 1968). PSHA is used for mapping the probability of exceeding a certain amount of ground shaking for a certain time period. For conventional PSHA it is standard to design the models for time intervals of 50 years. Even very low probabilities may be critical for these long-term hazard estimations, as it is these numbers that are

used to create building codes and earthquake insurance rates.

To estimate the seismic risk of aftershocks, the extended ETAS models are used to perform a large number (2000) of forward simulations, covering the area of interest during a time interval of 365 days after the mainshock. The same ETAS parameters are used as for the likelihood estimation (see Table 2.4). The spatial distribution of direct aftershocks is thereby modeled by additional source information, secondary events are modeled using the empirical spatial ETAS kernel (detailed descriptions in chapter 2.1). The background seismicity is modeled as a stationary Poisson process with constant occurrence rate μ. Additionally a frequency–magnitude distribution based on Gutenberg–Richter b–value of 1.0 is assumed and the maximum aftershock magnitude is limited to 1.2 magnitudes less than the mainshock magnitude because this hazard analysis is intended to take account of aftershock contributions only. The magnitude limitation follows the Båth's law which states that the magnitude of the largest aftershock in a sequence is usually 1.1–1.2 magnitudes less than the magnitude of the mainshock (Bath 1965).

The next step is to estimate the expected peak ground acceleration (PGA) for every event, for this purpose the ground motion model by Campbell and Bozorgnia (2008) is utilized. This model was developed as part of the PEER Next Generation Attenuation (NGA) project. The authors consider their model to be appropriate for estimating PGA for shallow continental earthquakes occurring in western North America and other regimes of similar active tectonics. Determining the probabilistic seismic hazard at a particular site requires the estimation of $P(pga \geq pga^* \text{ in } T)$, the probability of exceeding a predefined ground acceleration at least once during a certain time interval T.

For a large number N of simulated catalogs, the probability of non-exceeding a ground motion of pga^* during time T is obtained by counting those intervals in

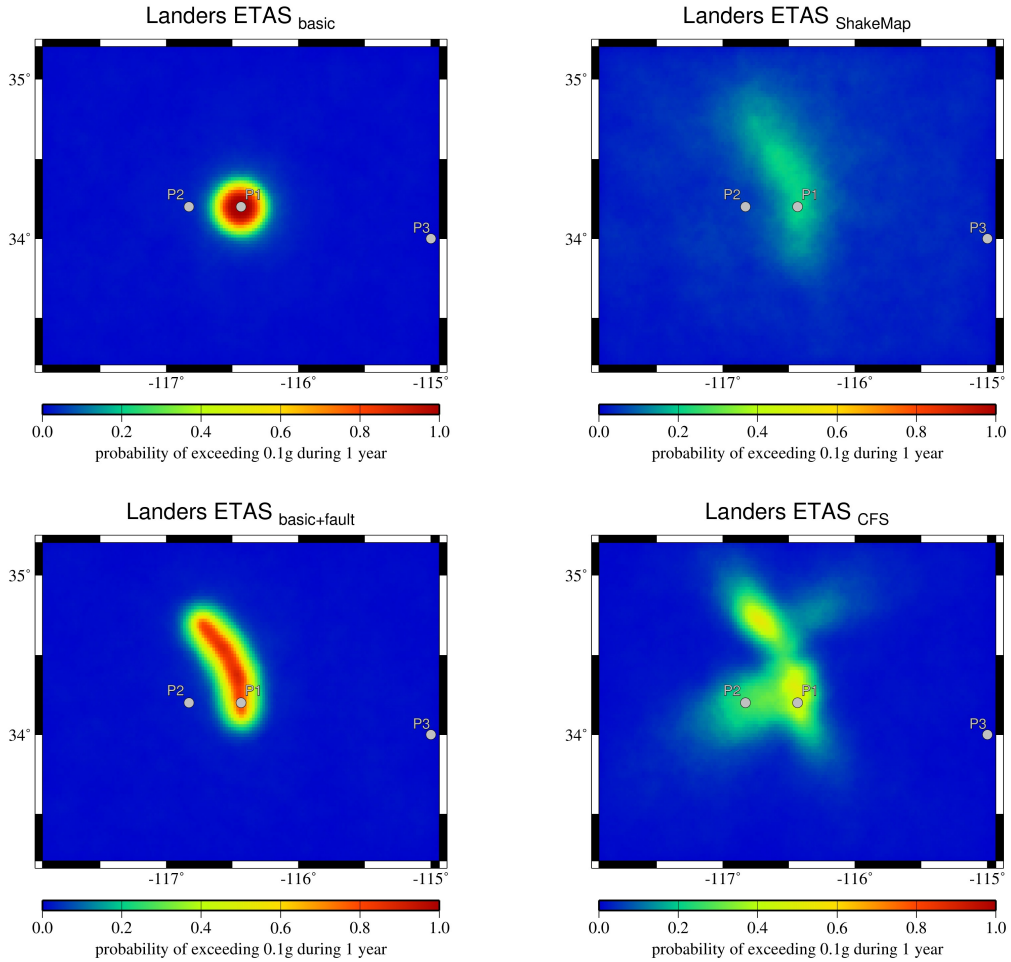

Figure 2.12: The seismic hazard maps for $ETAS_{\text{basic}}$, $ETAS_{\text{basic+fault}}$, $ETAS_{\text{ShakeMap}}$, and $ETAS_{\Delta\text{CFS}}$ models show the probability of exceeding a ground acceleration of 0.1g during 365 days after the mainshock. The $ETAS_{\text{basic}}$ and $ETAS_{\text{basic+fault}}$ models show high probabilities very focused around the mainshock epicenter and fault. Using the $ETAS_{\text{ShakeMap}}$ model, probabilities are much lower and stronger distributed on the map. The $ETAS_{\Delta\text{CFS}}$ leads to high probabilities close to the fault and two lobes in the north-east and south-west. P1 is the epicenter of the mainshock, P2 the epicenter of the Big Bear aftershock, P3 a location aside aftershock activity.

which pga^* has not been exceeded (Beauval et al. 2006):

$$P(pga^*, T) \;=\; \lim_{N \to \text{inf}} \frac{1}{N} \sum_{i=1}^{N} H(pga^* - pga_{max,i}(t)) \;. \tag{2.9}$$

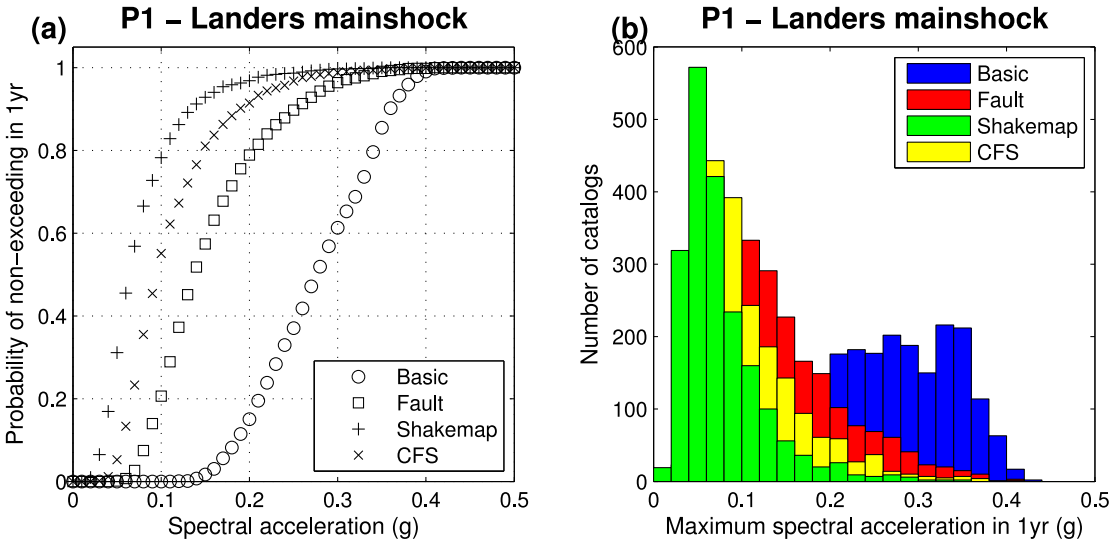

Figure 2.13: Computed probabilistic hazard for $ETAS_{\text{basic}}$, $ETAS_{\text{basic+fault}}$, $ETAS_{\text{ShakeMap}}$, and $ETAS_{\Delta\text{CFS}}$ models at the position of the Landers mainshock epicenter (P1). **(a)** Probabilities of non-exceeding the given acceleration during 1 year. **(b)** Distribution of maximum acceleration observed in the 2000 synthetic 1–year catalogs.

N is the number of catalogs, $pga_{max,i}$ is the maximum ground motion occurring at the site caused by events from the ith catalog, and H is the Heavyside function. As a result, the complement of $P(pga^*, T)$ is the probability that pga^* is exceeded at least once in the time interval T. According to Beauval et al. (2006) it is equivalent and faster to consider the distribution of maximum accelerations $pga_{max,i}$ and to calculate the probability of non–exceeding an acceleration level directly from this distribution. Note that in order to get stable results for high probabilities of non-exceeding, the number of synthetic catalogs has to be large.

Resulting hazard maps based on the $ETAS_{\text{basic}}$, $ETAS_{\text{basic+fault}}$, $ETAS_{\text{ShakeMap}}$, and $ETAS_{\Delta\text{CFS}}$ model for the Landers earthquake are shown in Figure 2.12. These maps reveal that for the $ETAS_{\text{basic}}$ and $ETAS_{\text{basic+fault}}$ models high risk is very focused around the epicenter and the fault trace, respectively. Contrastingly, the seismic risk predicted by the $ETAS_{\text{ShakeMap}}$ model is much more unfocused, probabilities close to the fault are much lower. The hazard map based on the $ETAS_{\Delta\text{CFS}}$

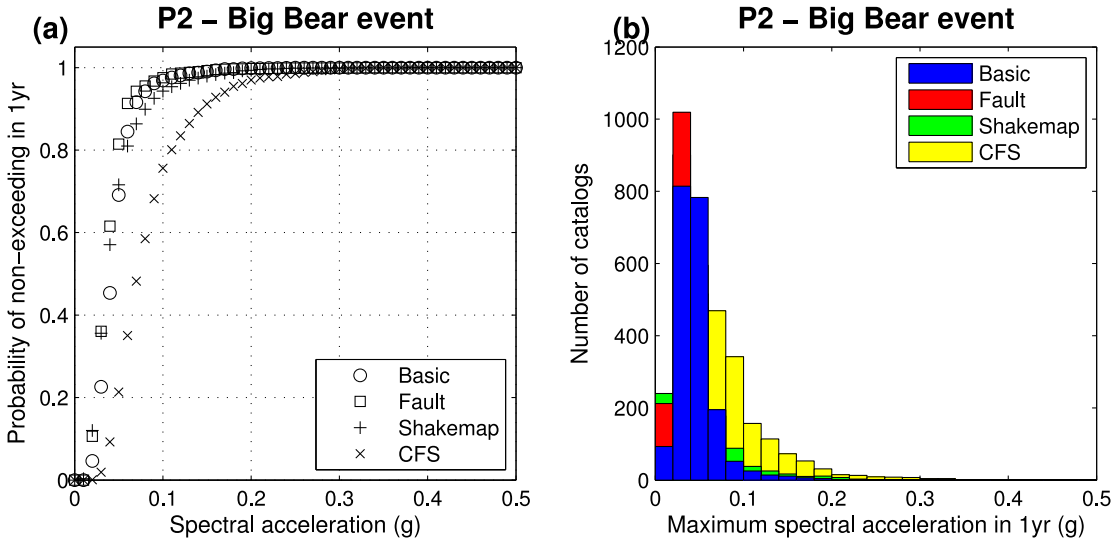

Figure 2.14: Same as Figure 2.13, but for the location of the Big Bear event (P2), the largest aftershock in the Landers aftershocks sequence.

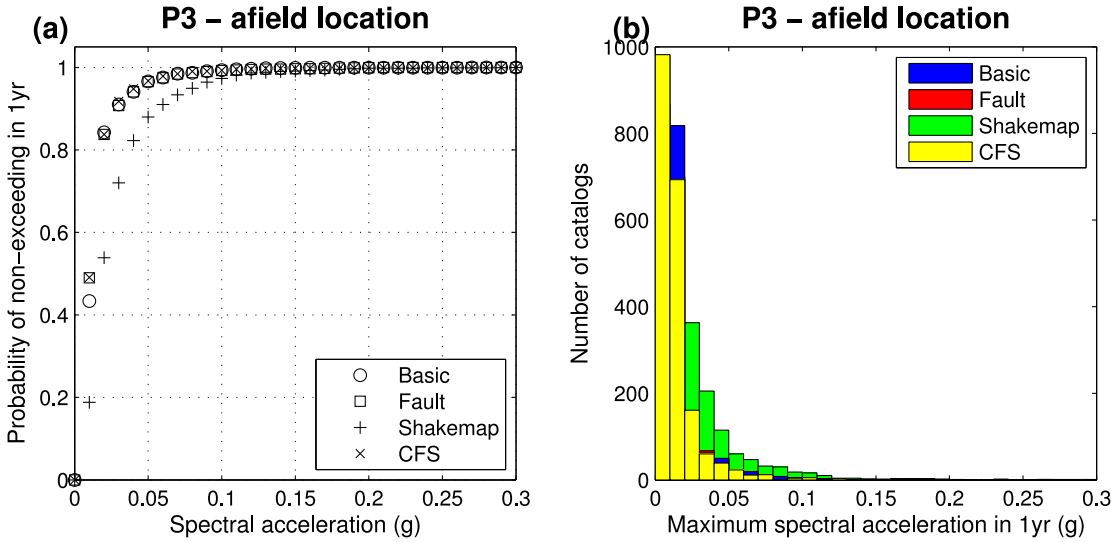

Figure 2.15: Same as Figure 2.13, but at a position afield the mainshock rupture (P3).

model has a more irregular shape, two lobes in the north-east and south-west suggest seismic risk off the actual fault trace.

Figures 2.13, 2.14 and 2.15 show the probabilities of non–exceeding an acceleration during 1 year and the distribution of maximum acceleration observed in the 2000 synthetic 1-year catalogs. The displayed curves represent the hazard

at one specific point predicted by $ETAS_{\text{basic}}$, $ETAS_{\text{basic+fault}}$, $ETAS_{\text{ShakeMap}}$, and $ETAS_{\Delta\text{CFS}}$ model. The curves in Figure 2.13 are calculated for position P1 of the Landers mainshock, curves in Figure 2.14 for position P2 of the largest aftershock (Big Bear M6.4), and curves in Figure 2.15 for position P3 away from the mainshock rupture. The $ETAS_{\text{basic}}$ predicts probabilities close to zero of non–exceeding an acceleration of 0.1g at position P1, the other models range between 0.2 and 0.8. However at position P2 where the largest aftershock occurred, the estimations based on the $ETAS_{\Delta\text{CFS}}$ model give the best estimations. A non–exceeding of 0.1g is given with a probability of 0.8. At position P3 all models predict high probabilities of non–exceeding accelerations of more than 0.1g, only the ShakeMap based model predicts slightly lower probabilities. Figures 2.13b, 2.14b and 2.15b show the corresponding distribution of maximum acceleration observed at both positions. In plot 2.13b the prediction of higher ground acceleration by the $ETAS_{\text{basic}}$ model compared to the others becomes even more obvious. Plot 2.14b shows that a larger number of synthetic catalogs based on $ETAS_{\Delta\text{CFS}}$ result in a ground acceleration larger than 0.1g. And in plot 2.15b it is shown that more synthetic catalogs based on the ShakeMap model than all other models lead to an exceeding of 0.1g.

2.5 Discussion

Investigating the performance of the models for three earthquake sequences revealed the importance of knowing the mainshock rupture geometry for aftershock forecasting. Based on this information only, the ETAS model can for two sequences best explain the near–fault aftershocks when the empirical seismicity based decay is evaluated as a function of the shortest distance to the mainshock rupture, i.e. the $ETAS_{\text{basic+fault}}$ model. The high information gain reveals the importance of a fast estimation of the fault geometry after a mainshock. This could be realized for example by fitting the locations of first aftershock recordings. That is already done in some aftershock models as in particular ETAS implementations (Helmstetter et al. 2006, Werner et al. 2011) and the STEP model (Gerstenberger et al. 2005).

Although ground motions decay with a similar decay law as used in the $ETAS_{\text{basic+fault}}$ model, the models based on ground motion are found to describe the aftershock distributions worse in most cases. An explanation could be the different gradients of the decay laws (Figure 2.8). The seismicity based probability decay (equation 2.2) proceeds much faster with increasing distance to the fault than the PGV values used in the models $ETAS_{\text{ShakeMap}}$ and $ETAS_{\text{GMM}}$. Thus in the $ETAS_{\text{basic+fault}}$ model more aftershocks are expected to occur in the vicinity of the fault than in more distant areas, this seems to be true (Figures 2.5d, 2.6d, 2.7d).

On the other hand, the results of the test only considering aftershocks more than 5 km distant to the fault show a worse performance of the $ETAS_{\text{basic+fault}}$ model compared to the models based on ground motions or ΔCFS. In particular, the models based on Coulomb stress change maps are found to perform best for the more distant aftershocks, this is in agreement with King et al. (1994). In larger distance to the fault, stress calculations are less affected by small–scale slip variability which is not resolvable by inversion of observational data and thus expected to be more accurate. This might explain why the static stress triggering

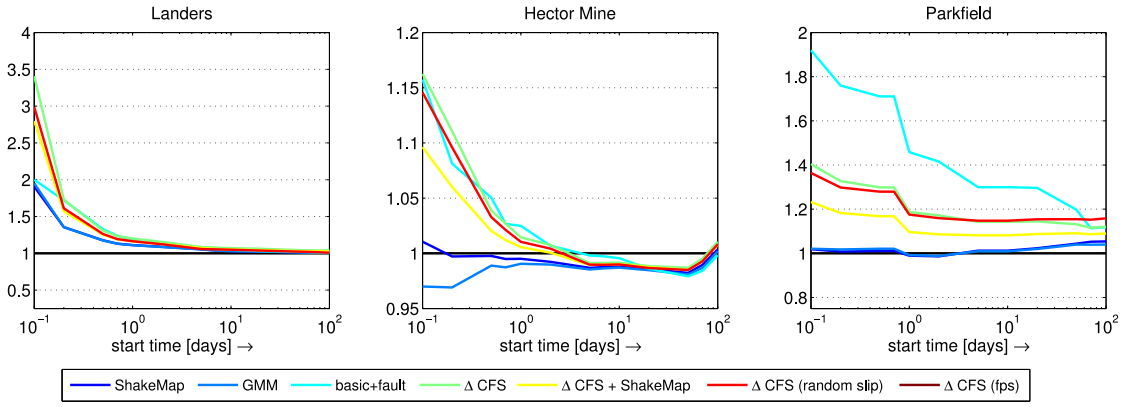

Figure 2.16: Results of the forecast test Test-A as a function of time. The plot shows the probability gain per event as a function of the start time (the end of the analyzed time window is always 365 days).

model works better for the more distant events than for the near–fault aftershocks. Using randomized slip distributions for the Coulomb stress calculations in all cases leads to very similar results like published slip model based stress calculations. This is promising because in the first case no additional information besides rupture geometry and earthquake magnitude is needed.

Additional tests were performed to exclude influences on the results by possible incomplete recordings of first aftershocks. For that the information gain was analyzed using different starting times of the testing period, in particular $S = 1$ day and 10 days in equation 2.8, and thus excluding the first, probably incomplete recorded events. It is found that the probability gain per event slightly decreases, but the relative order of the models remains the same. Another test also focuses on the start time S of the forecast interval, but allowing first aftershocks which occurred in the period [0, S] days to influence the aftershock probability. This reflects the case that the forecast is updated after the occurrence of the first aftershocks. When changing the start time from $S = 0.1$ up to 100 days, the probability gain per event decreases significantly after the first days and slowly for the next weeks (Figure 2.16). This is likely related to the fact that the $ETAS_{\text{basic}}$ model adapts to the anisotropic aftershock distribution by using the first aftershocks. The after-

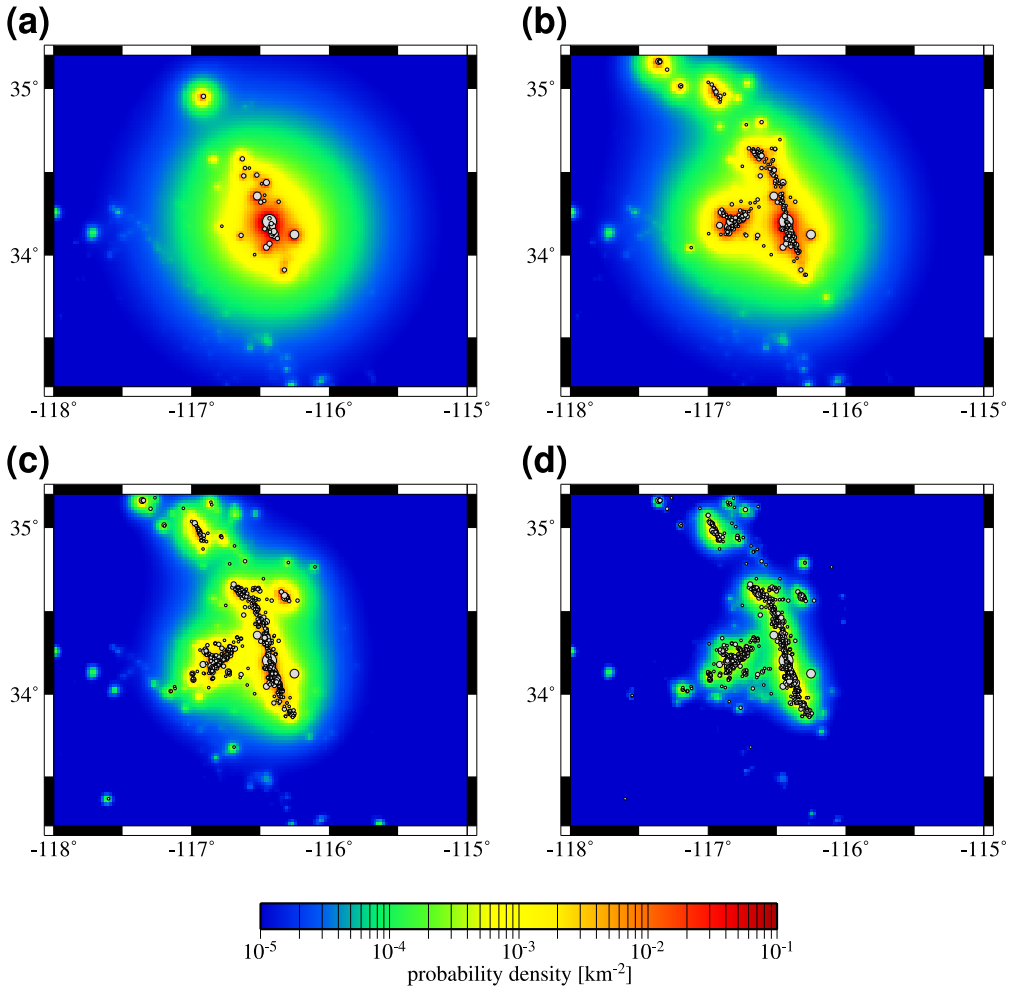

Figure 2.17: Estimated aftershock rate forecast for the Landers case based on the purely statistical isotropic ETAS model for different times (a) 0.1 days, (b) 1 day, (c) 10 days, (d) 100 days. Gray dots represent the aftershocks which occurred until this time.

shock rate forecast calculated for the $ETAS_{\text{basic}}$ and $ETAS_{\text{CFS}}$ models confirms this behavior (see Figures 2.17 and 2.18). For later times, the rate forecasts are almost the same. Clearly visible also the influence of the Omori–Utsu law on the ETAS rate forecast, for increasing time the probability density distribution dominated by the mainshock rate forecast becomes smaller and smaller.

Having included enough data ($S = 100$ days), the forecast becomes very similar to the $ETAS_{\text{basic+fault}}$ model. Then the performance of all models is very similar,

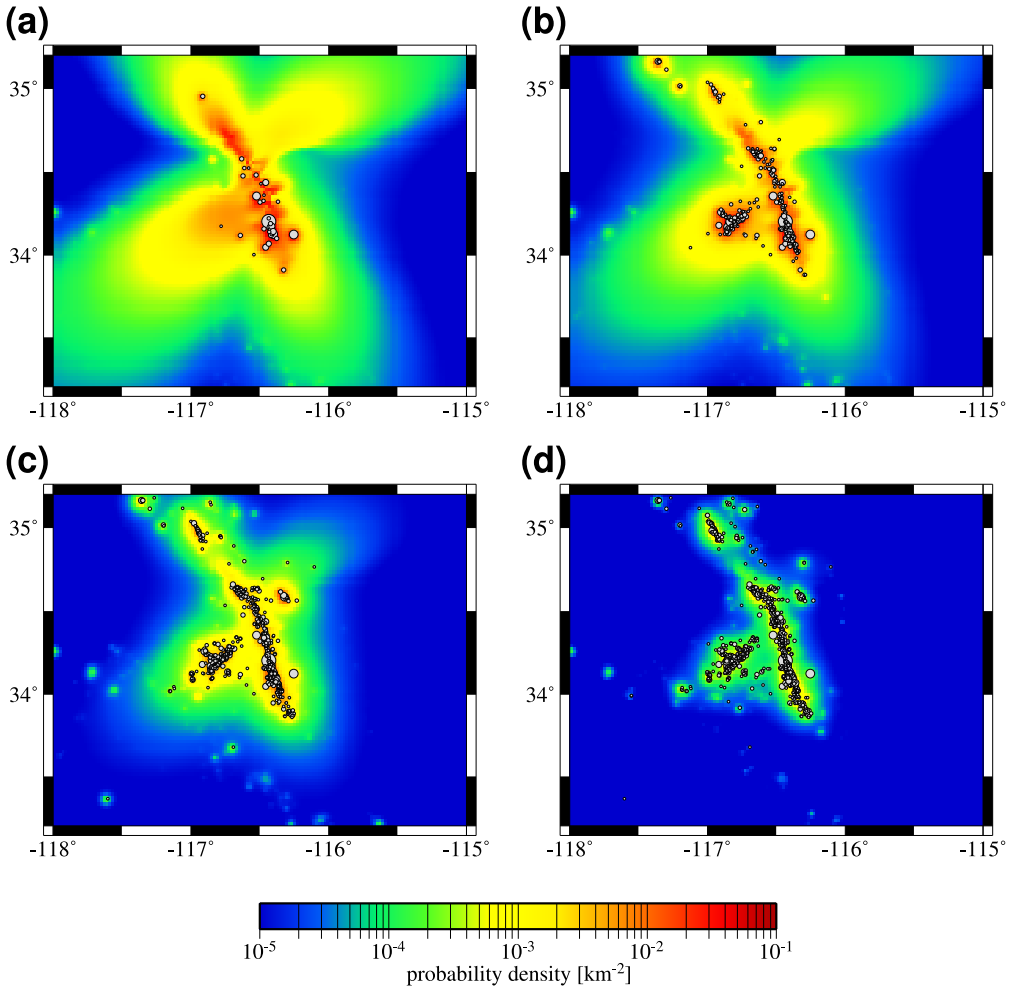

Figure 2.18: Same as Figure 2.17, but for the combined $ETAS_{\mathrm{CFS}}$ model.

although the static stress triggering model performs in all cases slightly better than the other models. This might be related to the increasing relative number of events occurring more distant to the fault for later times (see Figure 2.20 left).

Additional tests showed, that the models are also quite robust concerning different target magnitudes (Figure 2.19). The probability for the hybrid models is increasing for larger cut–off magnitudes, the relative order of the models generally remains constant, just for the Landers sequence the $ETAS_{\mathrm{basic+fault}}$ model performs worse for larger cut–off magnitudes. The right plot of Figure 2.20 reveals, that larger magnitude events occurred more distant to the fault in the case of the

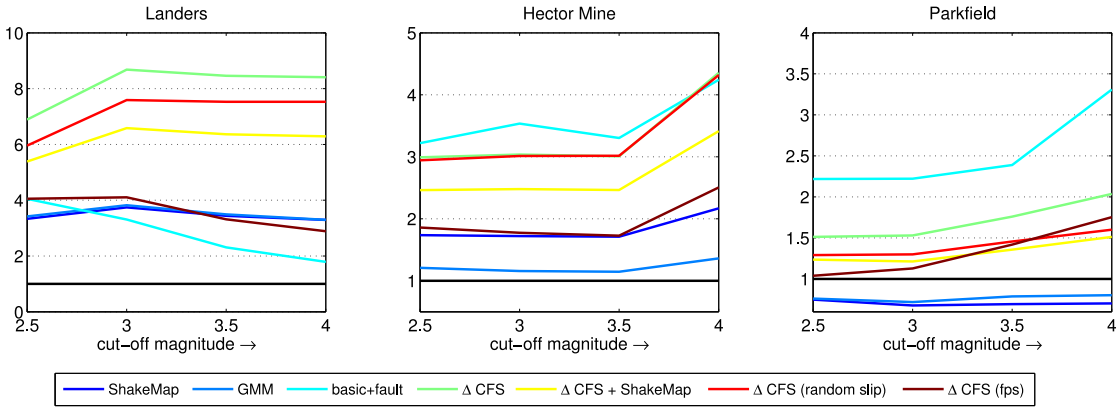

Figure 2.19: Results of the forecast test Test-A as a function of cut–off magnitude. The plot shows the probability gain per event as a function of the cut-off magnitude.

Landers and Parkfield sequence, and vice versa for the Hector Mine sequence.

The α values inverted using pre–mainshock events (Table 2.4) are quite low, this might also influence the results. To exclude an influence on the results, all calculations were repeated for the case that only μ, K, c, p, q and d were optimized from the precursory seismicity while the α value was fixed to 1.84 (corresponding to a value of 0.8 for basis of 10). No significant differences of the results were found. Different time intervals for the parameter inversion were also tested. The parameters change slightly. However, larger optimization intervals should be preferred, because more stable results are expected in that case. Concerning the tests, the different parameter estimations only slightly affect the probability gain of the models without changing the relative order of the different models.

Both tests indicate the robustness of the general findings against variations of particular ETAS parameters. To verify the results, the probability gain for 1000 model setups is calculated where the parameters were selected randomly from a normal distribution with mean and standard deviations displayed in Table 2.4. All parameters are allowed to vary at the same time. Because parameter correlations are not considered, the estimated standard errors may be overestimated. The error bars in Figures 2.9 and 2.10 show the interval between the 16% and 84% quantiles

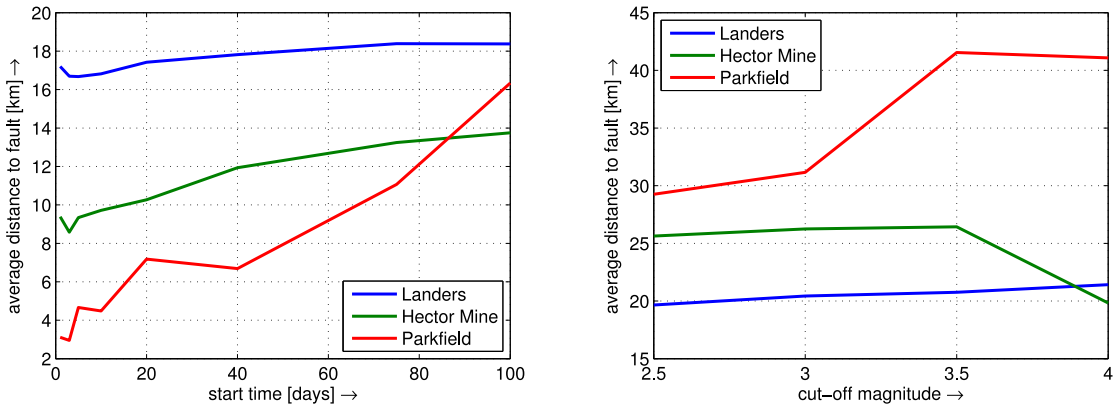

Figure 2.20: These plots show the average distance of all aftershocks at times larger than the start time (left plot) and for magnitudes larger than the cut–off magnitude (right plot). One can see that the later aftershocks occur more distant to the fault and larger magnitude events, except for the Hector Mine sequence, also occur more distant to the ruptured fault.

(1σ) of the resulting values. The probability gain differences are strongly correlated and the probability gain values vary almost simultaneously for all models when the ETAS parameters are changed. This is confirmed by linear correlation coefficients of more than 0.8 for Test–A.

It is interesting to note, that the static stress triggering model is found to outperform the ground motion models in almost all cases. Furthermore, it is found that the forecast ability of the ΔCFS model does not increase by combining it with dynamic stress maps. Also using different weights for the kernels could not improve the results much and no optimal weight could be found consistent for all aftershock sequences. This seems to indicate that static stress changes are the dominant physical mechanism for aftershocks, while dynamic stress triggering might only play a minor role for aftershock triggering, in agreement with previous conclusions (Hainzl, Brietzke and Zöller 2010). However, the result that the near–fault aftershocks are mostly best modeled by a simple decay function from the rupture area indicates that our incomplete knowledge of the rupture and the large uncertainties in the calculation of the stress change limit the forecast ability on short spatial scales.

The finalizing hazard analysis based on aftershock simulations revealed the differences in seismic risk at three different sites for the Landers case. One site is the mainshock epicenter where the $ETAS_{\text{basic}}$ model predicts the highest risk, the $ETAS_{\text{Shakemap}}$ model predicts the lowest risk. Calculating the ground acceleration based on the real aftershocks leads to a maximum value of 0.25g for that specific point. This point is actually less important for hazard assessment, because it is well known that there is aftershock hazard close to the mainshock epicenter. More interesting are areas further away from the epicenter. For this work hazard curves for two more places are calculated, the place where the later Big Bear event occurred and one point away from the fault, where no high aftershock activity was observed. Figure 2.5e showing the Coulomb stress based aftershock probability map already gave the hint, that this model quiet well explains the position of the Big Bear aftershock cluster. And as a result also the probabilities of non–exceeding a ground motion of 0.1g for the $ETAS_{\text{Shakemap}}$ model are lowest compared to the other models. At the afield location (P3) the hazard curves are very similar for all models, just the ShakeMap based model predicts slightly lower non–exceeding probabilities. Note that no aftershocks at all were recorded in that area.

The simulation based hazard estimation is an important tool for analyzing the seismic aftershock hazard at specific sites of interest. This could be very densely populated areas or vulnerable buildings. The necessary calculations are comparably fast and give a quick estimate of the expected hazard at the investigated place.

3 Information content of slip models with regard to aftershock forecasting

Testing the extended ETAS models described in chapter 2.1 revealed that including Coulomb stress change maps to model the spatial distribution of direct aftershocks markedly improves aftershock forecasting. Still, the stress calculations contain large uncertainties, like non-unique slip inversions. This can result in a number of published slip models for the same event, which differ in geometry and slip distribution. Comparing the results of the models $ETAS_{\Delta\mathrm{CFS\ (randomslip)}}$ and $ETAS_{\Delta\mathrm{CFS}}$ revealed that the difference is very small and in some cases the use of random slip might even be able to better forecast the aftershock distribution than by using published slip distributions.

In this chapter published slip models are compared to random slip models in order to address the information content of those inversions with respect to aftershock forecasting. Therefore the calculated stress change is converted into an aftershock probability map and related to the aftershock distribution using the $ETAS_{\Delta\mathrm{CFS}}$ model, for which more detailed descriptions can be found in section 2.1.4. The relative number of random models performing better than the published slip model is the quantity used to compare the performance of several published slip models. The aim is also to find similarities and differences in the published slip models which may explain good or bad performance in the tests. Though the influence

on the results by randomly varying the slip distribution is investigated, as well as the influence of changing the fault geometry or slip patch (subfault) resolution.

3.1 Data

Several different published slip models for a number of large earthquakes are used to investigate their usefulness for aftershock forecasting. The mainshocks are, like in the first part of this work, the 1992 Landers, the 1999 Hector Mine, and the 2004 Parkfield earthquake. For each of them several slip models are tested. For the Landers earthquake, four slip models are analyzed, each of them with three segments and patch resolutions between ∼3x3 km and 5x5 km. For the Hector Mine mainshock two published slip models are investigated, one with three and the other one with four segments. Both have slip resolutions of ∼3x3 km. Three models describe the slip distribution of the Parkfield event, all of them having one segment and patch resolutions ∼2x2 km. More detailed information about the used slip models are listed in Table 3.1, plots of all used reference slip distributions are added to the Appendix. The earthquake catalog data used for the aftershock forecast tests is taken from the relocated catalog by Hauksson et al. (2012) for Southern California.

3.2 Methods

Detailed description of Coulomb stress calculations are given in section 2.1.4. Equally to the descriptions given there, also in the following tests uncertainties are considered by randomly selecting the strike, dip and rake values of the receiver planes for a large number of stress change maps based on randomized slip distributions. In each case, the stress change is resolved on fixed receiver planes. Also the clock advance model introduced by Hainzl, Brietzke and Zöller (2010) is utilized to convert the stress changes to an aftershock probability map.

Table 3.1: Information related to the used slip models giving the input data used for the inversion process, the number of segments, their size, strike and dip, and subfault resolution.

Model (Input Data)	Number of Segments	Segment Size	Strike/Dip of Segment	Patch Resolution
Landers				
Wald and Heaton (1994)	3	30x15 km	355°/90°	3x5 km
(GPS, strong motion,		27x15 km	334°/90°	3x5 km
surface offset)		36x15 km	320°/90°	3x5 km
Cohee and Beroza (1994)	3	27x18 km	354°/90°	3x3 km
(strong motion)		30x18 km	331°/90°	3x3 km
		45x18 km	322°/90°	3x3 km
Cotton and Campillo (1995)	3	25x15 km	354°/90°	5x5 km
(strong motion)		25x15 km	331°/90°	5x5 km
		30x15 km	322°/90°	5x5 km
Hernandez et al. (1999)	3	25x15 km	355°/90°	5x5 km
(InSAR, GPS,		25x15 km	339°/90°	5x5 km
strong motion)		30x15 km	317°/90°	5x5 km
Hector Mine				
Ji et al. (2002a)	3	33x16.2 km	346°/85°	3x2.7 km
(GPS, strong motion,		21x15.4 km	322°/75°	3x2.6 km
surface offset)		30x16.2 km	325°/85°	3x2.7 km
Salichon et al. (2004)	4	30x18 km	346°/86°	3x3 km
(InSAR, GPS,		18x18 km	321°/75°	3x3 km
teleseismic)		12x18 km	320°/80°	3x3 km
		12x18 km	342°/80°	3x3 km
Parkfield				
Custódio et al. (2005)	1	40x15 km	140°/87°	1.9x1.7 km
(strong motion)				
Dreger et al. (2005)	1	34x15.5 km	137°/80°	1.9x1.7 km
(GPS, strong motion)				
Ji et al. (2004)	1	40x14.5 km	137°/83°	2x1.5 km
(GPS, strong motion)				

The random slip models are constrained by the geometry of the published slip model and the magnitude of the earthquake. Slip is tapered towards the margins

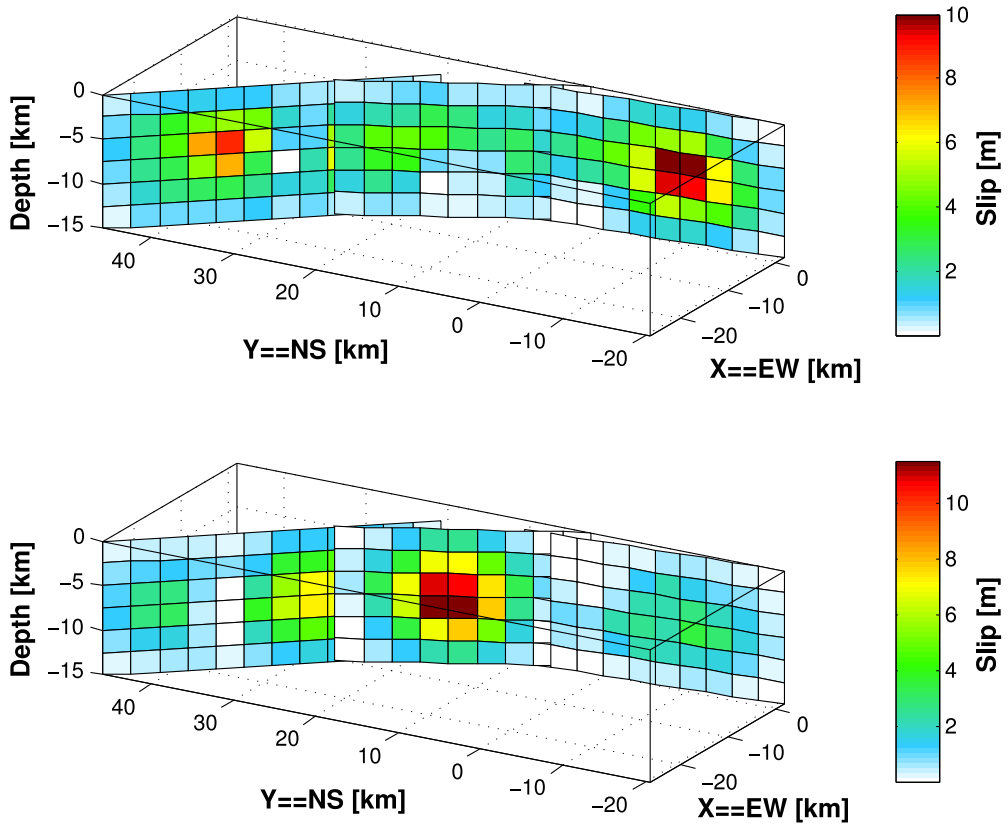

Figure 3.1: Two random slip realizations based on the geometry of the Wald and Heaton (1994) slip model.

using a cosine function in the range $[0, \frac{\pi}{2}]$ and high frequencies are damped. Differently from the previous tests, here the random slip model based stress change maps are not constrained by a large number of slip realizations but a large number of stress change maps related to different receiver mechanisms is calculated based on one, always different, random slip model. The random slip realizations vary within the given constraints. That is the k^{-2} slope to damp high frequencies, which allows a few larger slip patches per segment. The size of the slip patches scales with the event magnitude. The geometry of the slip model, that is the size and orientation of the segments and resolution of the single patches, is fixed in the first part of that work. Two examples how random slip realizations might look like are shown in Figure 3.1 for the Landers case. These models have one or two

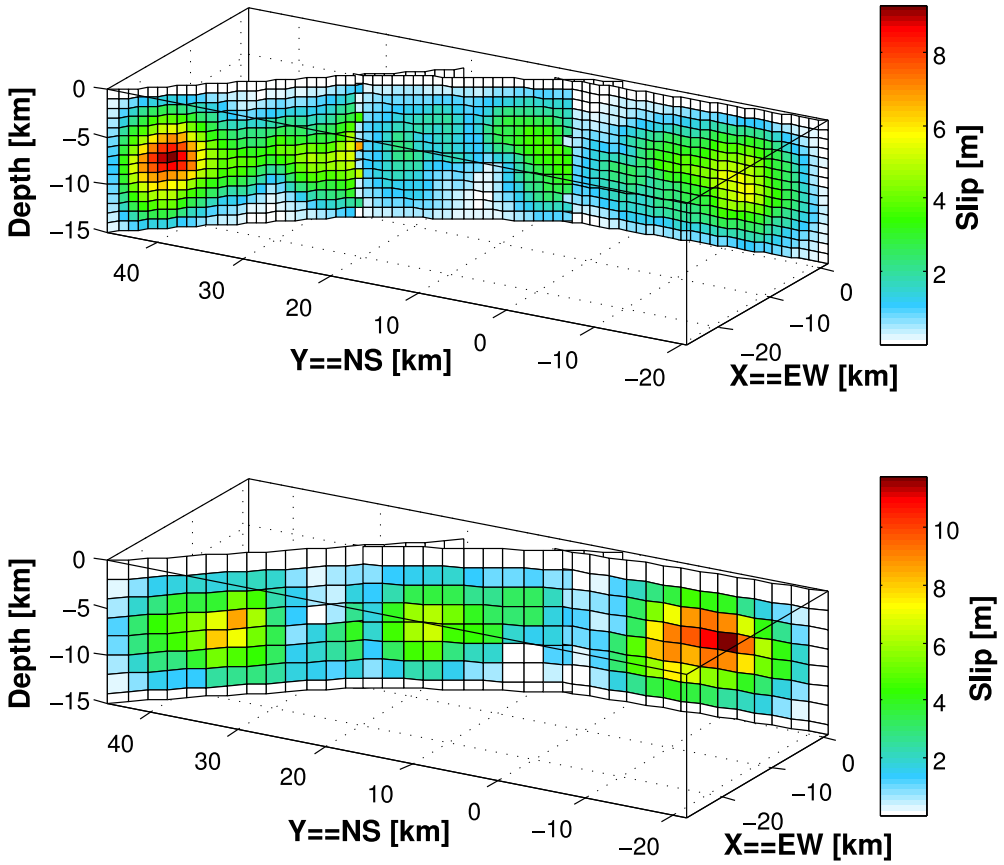

Figure 3.2: Two random slip realizations with patch resolutions of 1x1km and 2x2km, based on the geometry of the Wald and Heaton (1994) slip model.

large slip patches per segment. The average slip per segment is not equal but also varies randomly. That can result in segments having very high slip and segments with very low slip. Due to the tapering, the slip is low towards the margins. The geometry and resolution in this example is exactly the same like the Wald and Heaton (1994) slip model.

In this part, calculations are based on the formulations of Okada (1992). If uncertainties are considered, like done in this work, the differences of stress change maps based on the code of Wang et al. (2006) and Okada (1992) are very small. The reason to use his formulations here is that the code is computationally much more efficient. He presents in his publication a complete set of analytical expressions for

internal deformation and strains due to shear and tensile faults in a homogeneous half space for finite rectangular sources. These expressions are a powerful tool for observational and theoretical analyses of static field changes associated with earthquakes and have been applied in numerous studies. The calculations for static stress change are divided into two parts. Firstly, the stress tensor at the observation point is calculated. This requires the knowledge of crustal properties, here average properties are used (density $\rho = 2700\,\mathrm{kg/m^3}$, p– and s–wave velocities $v_p = 5500\,\mathrm{m/s},\ v_s = 3200\,\mathrm{m/s}$). In the second step, normal and shear stress change is calculated by solving the stress tensor on the receiver plane. This division into two parts makes the software used here very efficient, because the stress tensor has to be calculated only once for different receiver fault orientations.

Published slip models usually have quite different subfault resolutions. The resolution defined for the slip model inversion depends on the sensitivity of input data at depth. The resolution decreases for larger depth and differs depending on the input data, e.g. the slip resolution based on geodetic data is much better than of teleseismic data (Salichon et al. 2004). Though the teleseismic data is just used to constrain the temporal evolution of the rupture process. Different patch resolutions might influence the aftershock forecast test performed here. To investigate this influence, all tests are repeated using patch resolutions of 1x1km, 2x2km and 3x3km. As an example, Figure 3.2 shows two random slip realizations based on the fault geometry published by Wald and Heaton (1994). The subfault resolution is changed to 1x1km and 2x2km, the plot reveals, that the general slip patterns remain the same. Because slip is assumed to be self–similar and the size of the fractal slip is constrained by the seismic moment of the event, the general pattern is independent of the subfault resolution and therefore stays almost constant.

3.3 Test

In the test setup, the aftershock distribution is related to the theoretical static stress change calculated from random slip distribution. This is done by utilizing the extended $ETAS_{\Delta CFS}$ model introduced in chapter 2.1. The model relates the distribution of direct aftershocks to a stress change based probability map rather than to the standard ETAS spatial kernel. The ETAS model includes the influence of all previous events on the rate forecast of future events.

As this part of the work does not aim to forecast the aftershock distribution directly but to test the influence of changing properties of the slip models used for the forecasting, aftershock interactions are allowed according to the definition of the ETAS model. As ETAS parameters, standard values are chosen ($\mu = 0.05\,\mathrm{M} \geq 3$ events per day and unit area, $K = 0.021$, $c = 0.031$ days, $\alpha = 1.6$, $p = 1.06$, $q = 1.44$, $d = 0.048$ km) according to the parameters published by Woessner et al. (2011). Because the three investigated sequences occurred in the same tectonic setting in Southern California, and different parameter choices should not influence the results, the parameters are chosen to be equal for all tests.

The test quantity is the logarithmic likelihood relating the model to the one year aftershock sequences. For easily comparing the different models, probability gain per event $e^{\Delta lnL/N}$ has been calculated. Here, ΔlnL is determined relative to the $ETAS_{\Delta CFS}$ model based on the published slip model. This facilitates the comparison of the different models based on random slip and quantifies the improvement concerning the standard model. A probability gain value > 1 means, that this model performs better than the reference model, a value < 1 implies a worse performance of the model in describing the aftershock distribution.

In total, 100 stress change maps based on different random slip distributions were tested and compared to the corresponding published slip model. An average slip distribution was calculated from the 100 random slip models and also tested related to the reference model. And if there were models performing better than

the published slip model, these were combined to an average model and tested as well. This may give a hint on the general slip pattern which is preferred by the aftershock distribution. Additionally, the performance using a uniform slip model as input for the calculations was tested.

The published slip models not only differ in terms of slip distribution but also in terms of subfault resolution and fault geometry. To estimate the influence of these parameters, one test focuses on changing the subfault resolution between 1x1 km and 3x3 km. Another test focuses on changing the fault geometry. The geometry is changed randomly by selecting the strike and dip values from a Gaussian distribution using the originally published strike and dip values and a standard deviation of $\sigma = (5°, 10°, 20°)$. If the slip model has more than one fault segment, the new strike and dip values are selected independently for every segment. For changing the strike, the segment plane is rotated around the vertical axis going through the plane center. For changing the dip, the plane is rotated around the horizontal axis defined by the upper edge of the plane. In some cases during the slip model inversion process, the upper edge of the fault geometry is defined by surface offsets. Therefore by fixing the upper edge during rotation, this information is kept. The models are compared to the originally published slip model.

3.4 Results

Relating slip models to the aftershock distribution with help of an ETAS based approach results in a comparison of the aftershock forecast ability of random slip models with the corresponding published slip model. Figure 3.4 shows the histogram obtained from calculations based on the Landers aftershock sequence and the Wald and Heaton (1994) slip model. The results show, that 85% of the random slip distribution based models perform better than the model using the published slip distribution. The distribution is rather uneven, most models range between 0.99 to 1.05 probability gain. The plot also shows, that the model using a uniform slip distribution as input for the stress calculations (green dot) performs slightly better compared to the reference model. Also using an averaged slip model combining all random slip models (red dot) or only random slip models having probability gain > 1 (orange dot) both increase the aftershock forecast. The slip distributions of both average slip models reveal, that the average models, including a large enough number of slip models, represent the used taper function (Figure 3.3). Both average models are very similar, because most of the random models perform better than the reference model and are therefore included in both average models.

If the number of simulations is increased to 1000 (Figure 3.5), one can see that the distribution is more even than the results of only 100 models (Figure 3.4) and very similar to a Gaussian distribution. 85.7% of the random models perform better than the reference model. The performance of both average models is almost the same like in the test where only 100 random models have been used.

The second example shows the histogram obtained from calculations using the Hector Mine aftershock sequence and the slip model of Ji et al. (2002a). All random slip models perform better than the published slip model. The uniform slip model performs slightly better, but worse compared to the random models. Both average models perform better than the reference model, their performance is exactly the

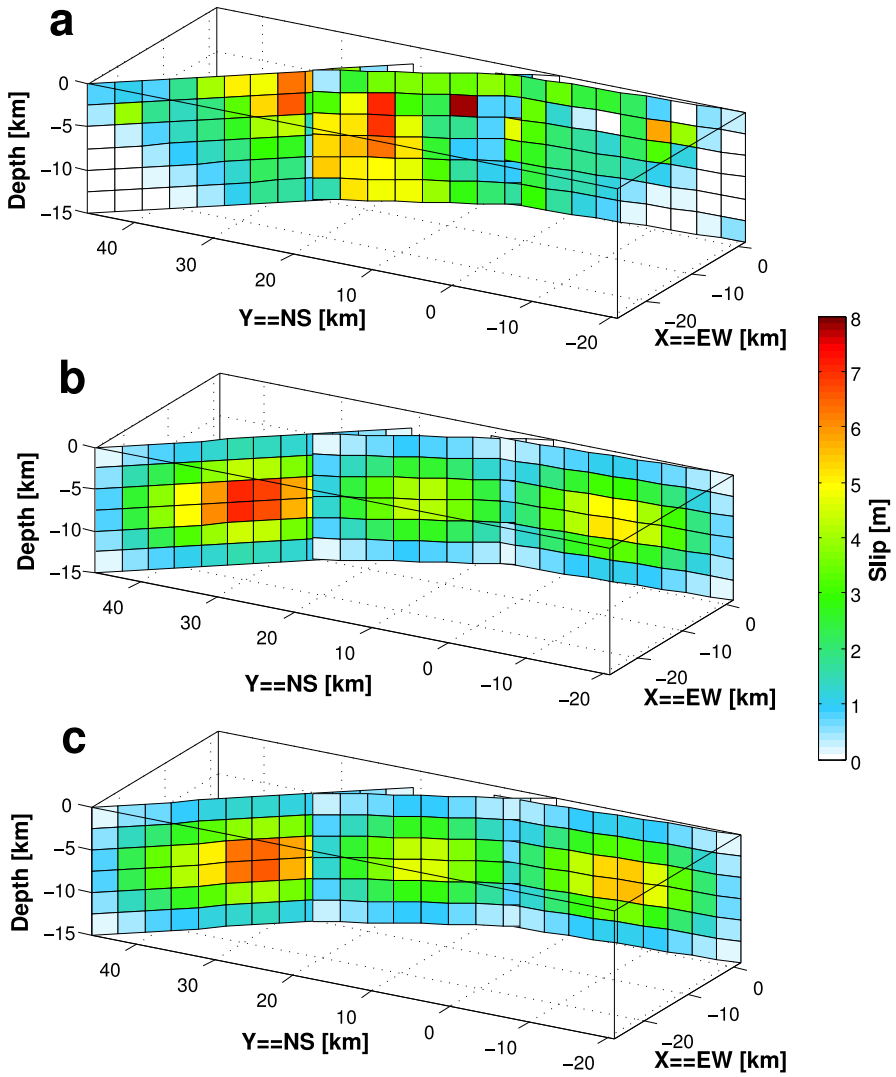

Figure 3.3: (a) original slip distribution by Wald and Heaton (1994), (b) average slip model of all random slip models, (c) average slip model of random slip models performing better than original model (probability gain > 1).

same, because all random models are included in both average models.

Details of all other tested slip models are summarized in Table 3.2. The results show, that the other three tested models for the Landers earthquake perform very well, only very few random models perform better than the published slip model. In the case of the Parkfield sequence, only very few random models are found to perform better than the published slip models. Contrastingly, all random models

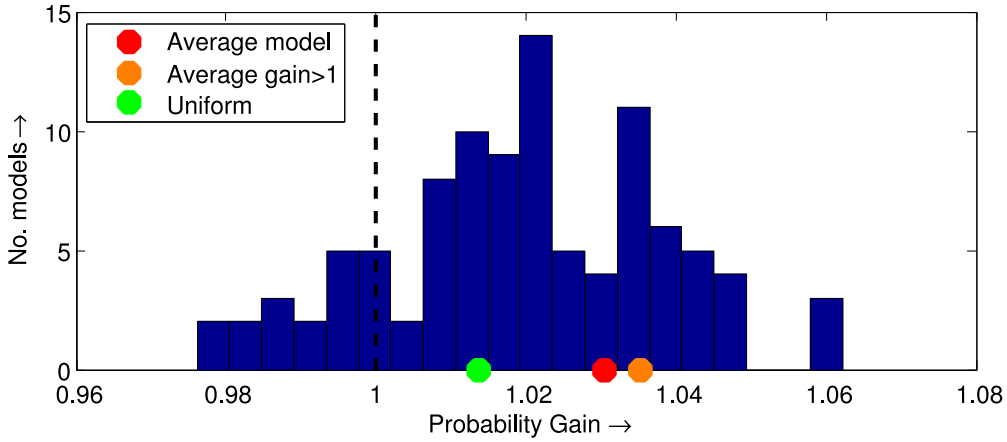

Figure 3.4: This plot shows the probability gain of the models using the stress change maps based on 100 different random slip distributions, relative to the published slip model by Wald and Heaton (1994) for the Landers earthquake. Additionally the colored dots represent the performance of the uniform slip model, the average slip model related to the average of all random slip distributions and the slip model being the average of only that slip models which have a probability gain > 1. The performance of the reference model (probability gain $= 1$) is indicated by a black dotted line.

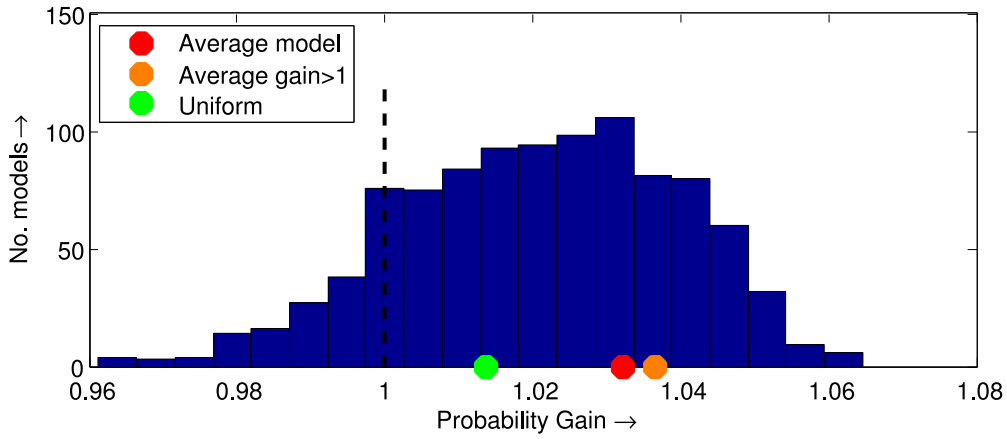

Figure 3.5: This plot shows the probability gain of the models using the stress change maps based on 1000 different random slip distributions, relative to the published slip model by Wald and Heaton (1994) for the Landers earthquake.

perform better than the two published slip models for the Hector Mine earthquake. Four of the nine average slip models perform better than the reference models, six average models based on the gain>1 models perform better than the reference

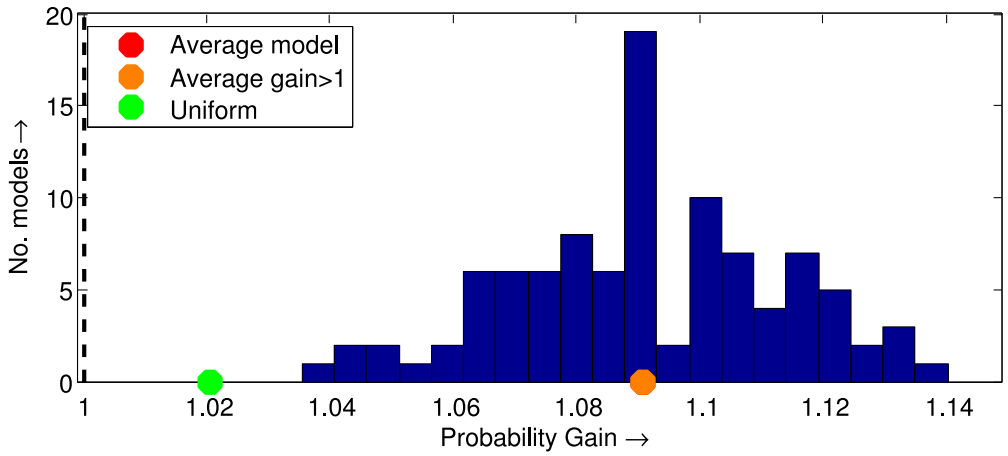

Figure 3.6: This plot shows the probability gain distributions of the 100 different random slip distributions for the Hector Mine event, relative to the published slip model by Ji et al. (2002a). The orange dot is on top of the red dot, because the performance of both random model is exactly the same.

models. There is no result for the first Parkfield model, because none of the random models performs better than the reference model. Additionally, almost all uniform slip models for the nine test cases perform worse than the reference model. Resulting probability density maps for all test cases are shown in the Appendix.

3.4.1 Changed subfault resolution

The results based on the published fault geometry differ a lot, while three of the tested published slip models for Landers and all tested models for Parkfield perform quite well compared to the random models, one of the models for Landers and the slip models for Hector Mine perform a lot worse. One reason could be the different subpatch resolutions of the slip models, which range between 1.9x1.7km to 5x5km. To estimate the influence of changed patch resolution, in the next test the patch resolutions are changed equally for all slip models and are fixed to 1x1km, 2x2km and 3x3km. The results are added to Table 3.2 in the last three columns. Except for the last two tested Parkfield model, the results are fairly stable. The performance of the random models is nearly the same, despite the

Table 3.2: This table gives the percentage of random models (out of 100) performing better than the published slip model with original subfault resolution and resolutions of 1x1km, 2x2km and 3x3km. Additionally the probability gain of the average slip model, the average of the models having probability gain > 1 and the uniform slip model is given.

	original resolution	average	average gain>1	uniform	1x1km	2x2km	3x3km
Landers							
Wald and Heaton (1994)	85%	1.033	1.037	1.014	91%	89%	87%
Cohee and Beroza (1994)	17%	0.970	1.008	0.974	40%	31%	17%
Cotton and Campillo (1995)	11%	0.983	1.017	0.989	15%	4%	10%
Hernandez et al. (1999)	25%	1.004	1.025	0.993	38%	9%	22%
Hector Mine							
Ji et al. (2002a)	100%	1.091	1.091	1.020	100%	100%	100%
Salichon et al. (2004)	100%	1.061	1.061	0.981	100%	100%	100%
Parkfield							
Custódio et al. (2005)	0%	0.872	-	0.712	0%	0%	5%
Dreger et al. (2005)	13%	0.884	0.946	0.727	94%	95%	100%
Ji et al. (2004)	6%	0.860	0.939	0.745	13%	66%	90%

changed subfault resolution.

3.4.2 Changed fault geometry

Steacy et al. (2004) already found that changing the fault geometry has a higher influence on the stress distribution than changing the slip distribution. The per-

Table 3.3: This table gives the percentage of random models (out of 100) performing better than the published slip model with original segment strike and dip and randomly selected strike and dip using a standard deviation of 5°, 10° or 20°.

		random strike/dip random slip distribution		
	original strike/dip	$\sigma = 5°$	$\sigma = 10°$	$\sigma = 20°$
Landers				
Wald and Heaton (1994)	85%	72%	34%	3%
Cohee and Beroza (1994)	17%	19%	11%	0%
Cotton and Campillo (1995)	11%	10%	5%	1%
Hernandez et al. (1999)	25%	9%	1%	0%
Hector Mine				
Ji et al. (2002a)	100%	98%	84%	65%
Salichon et al. (2004)	100%	100%	87%	45%
Parkfield				
Custódio et al. (2005)	0%	0%	0%	0%
Dreger et al. (2005)	13%	5%	2%	0%
Ji et al. (2004)	6%	8%	1%	1%

formed test described in this section addresses the influence of changing the strike and dip of fault segments.

This test reveals that changing the fault geometry strongly influences the performance of the random models (see Table 3.3). Using a standard deviation of $\sigma = 5°$ for strike and dip of the fault segments, the models performance is very similar to the test case for which the geometry is not changed. When the standard deviation is increased further (to 10° and 20°), all models consistently perform worse.

Additionally the behavior of models was tested where the geometry was changed as well, but the slip distribution is the same like the reference model (see Table 3.4).

Table 3.4: This table gives the percentage of models (out of 100) performing better than the published slip model with original segment strike and dip and randomly selected strike and dip using a standard deviation of 5°, 10° or 20°. All models use the original slip distribution.

		random strike/dip original slip distribution		
	original strike/dip	$\sigma = 5°$	$\sigma = 10°$	$\sigma = 20°$
Landers				
Wald and Heaton (1994)	85%	100%	71%	8%
Cohee and Beroza (1994)	17%	98%	72%	19%
Cotton and Campillo (1995)	11%	93%	53%	9%
Hernandez et al. (1999)	25%	93%	37%	3%
Hector Mine				
Ji et al. (2002a)	100%	100%	96%	74%
Salichon et al. (2004)	100%	100%	100%	84%
Parkfield				
Custódio et al. (2005)	0%	35%	15%	6%
Dreger et al. (2005)	13%	53%	16%	5%
Ji et al. (2004)	6%	62%	28%	7%

In this way, the influence of changed slip distributions on the results can be eliminated. Best results are obtained using a standard deviation for strike and dip values of $\sigma = 5°$. When the standard deviation is increased, the number of models performing better than the reference model decreases.

3.5 Discussion

The introduced methodology is able to be used for estimating the information content of slip models with regard to aftershock forecasting. All results rely on the assumption, that static stress triggering plays a dominant role in aftershock triggering. For the stress change calculations, uncertainties have to be taken into account, e.g. by using a Gaussian distribution for aftershock mechanims. Otherwise it is not possible to explain the aftershock distribution very well, in particular very close to the fault.

The results of the first test, which uses the fault geometry of a published slip model and randomized slip, reveal that for different slip models between 0% and 100% of the random models are found to perform better than the published slip model. On the other hand, the models using uniform slip distribution almost always perform worse compared to the reference model. No clear correlation between different types of input information for the slip model inversion and performance in the tests is found. Many of the slip models are based on similar datasets, still the slip distributions are very different. This could mean, that the applied inversion techniques have a larger influence on the slip distribution calculations.

The investigation of different subfault resolutions revealed that changing the subfault resolution to 1x1km, 2x2km or 3x3km in most cases only minimally influences the results. The reasons might be that the general slip pattern, of one or two large slip patches per segment which scale with moment magnitude, does not change using different subfault resolutions. Just if the resolution is very low, e.g. only one subfault per segment which corresponds to using uniform slip on the segment, the general slip patterns can not be reproduced anymore. In some cases, like the last two Parkfield models, the results change a lot. This seems to be a problem with the taper function, not dealing well with uneven subfault sizes. Choosing another taper function, e.g. based on a two dimensional Gaussian function, or not tapering at all gives much more reasonable results. For a resolution

of 1x1km the results then range between 1% and 10%, for 2x2km between 7% and 15% and for 3x3km between 4% and 37%.

The results using average slip models are quite promising. In some cases the results are better than using the original model, in most other cases the results are at least close to the original model. This implies, that very simplified slip distributions are already sufficient for first aftershock distribution estimations. Only in five out of nine tested cases, the inverted slip distribution better explains the aftershock pattern.

Another test also focused on the usefulness of uniform slip models. In that case, uniform slip was used for slip models consisting of more than one segment, but the amount of uniform slip was allowed to be different for each segment. The slip was estimated randomly, just the average slip of all segments scaled with moment magnitude. Only very few models were found to perform better than the reference model. This test confirmed, that uniform slip models are not very helpful for aftershock forecasting.

Steacy et al. (2004) already summarized that the geometry of the fault has a much larger influence on the stress change than the slip distribution on the fault. The next test confirms these observations, there the strike and dip angles of the fault segments were changed randomly using a standard deviation between 5° and 20°. The results, compared to the test where the geometry is constant, change a lot. If a standard deviation of 5° is used, the number of random slip models performing better than the reference model is highest. Whereas the random models perform worse, if the standard deviation is chosen higher. This implies, that the published fault orientations are already close to an optimal orientation with regard to the aftershock distribution and the true mismatch of the geometry for slip inversions is around 5°. If a low standard deviation is chosen in the test, many models fall within this optimal range. If the standard deviation is chosen too high, more models seem to be outside the optimal segment orientation.

4 Summary and Conclusions

In this work, I investigate the possibility and feasibility to improve ETAS type forecasts by incorporating additional mainshock information which might be available within minutes to hours after the events. The ETAS model has been established as a kind of standard model for short–time earthquake clustering over the past years. However, the spatial model component is rather unsatisfactory because it predicts only radially symmetrical aftershock clouds in clear contradiction to observations. This is because the basic ETAS model only relies on point information, namely the time, location and magnitude of the earthquake. Here, the benefit of including additional information is tested, e.g. rupture geometry, recorded ShakeMaps and static Coulomb stress changes.

The performed tests show, that the inclusion of additional input information can improve purely statistical aftershock forecasts in most cases. Furthermore, to describe the overall aftershock sequence best, only the fault geometry is needed. Evaluating the empirical aftershock decay kernel as a function of the nearest distance to the extended source instead of the epicenter leads to a significant improvement of the forecasts. Though a focus should be on estimating the fault geometry, either by using fault plane solutions, fitting the first aftershocks or applying other techniques. Because the largest aftershocks might be expected to occur on still unruptured neighboring known or unknown fault segments, including static stress changes in the ETAS model is very promising. However, the model based on ΔCFS information best performs for the more distant aftershocks. Random slip models could increase the availability speed of Coulomb stress calculations,

nevertheless further improvements in creating the random slip distributions, selecting subfault resolution or varying the fault geometry could improve the random slip based stress models. Finally, the tests show that dynamic stress triggering ($ETAS_{\mathrm{Shakemap}}$ and $ETAS_{\mathrm{GMM}}$ models) is only in few cases able to describe the observations better than the basic ETAS model. The performed tests consistently show that static stress triggering models outperform the dynamic stress triggering models (ground–motion models) in all cases. Though the tested sequences occurred in a strike–slip environment, in other tectonic regimes the results might be different.

Currently these models are implemented in CSEP (Collaboratory for the Study of Earthquake Predictability) for prospective testing and to compare the forecast ability to earthquake models of other research groups. CSEP supports a wide range of scientific prediction experiments in order to evaluate models in a predefined testing environment under the same conditions and constraints.

In the second part of my work the previously in chapter 2 introduced model $ETAS_{\mathrm{CFS}}$ is used to relate the modeled aftershock rate, based on previous seismicity and static stress change induced by the mainshock, to the aftershock distribution. In order to quantify the usefulness of published slip models, their performance is compared to random slip models. It is found that for some slip models none of the random models performs better than the published slip models, for other models all random models perform better.

One test intended to investigate the dependence of the slip model performance on the subfault resolution. In most cases, the performance was nearly the same like using the original resolution. This implies that the models are relatively robust concerning the subfault resolution. Just if the resolution is very low, e.g. in the case of uniform slip distributions, the performance in most cases is worse compared to the reference model.

The next test focused on changing the fault segment geometry, that means randomly varying the strike and dip values using a standard deviation between 5°

and 20°. The random slip models perform better for small standard deviations and worse for larger standard deviations. This could mean, that the original geometry is already close to the optimal geometry and if the standard deviation is chosen too hight, many models are outside this optimum range.

Bibliography

Aki, K.: 1993, Local site effects on weak and strong ground motion, *Tectonophysics* **218**(1-3), 93–111.
URL: *http://linkinghub.elsevier.com/retrieve/pii/004019519390262I*

Bach, C. and Hainzl, S.: 2012, Improving empirical aftershock modeling based on additional source information, *Journal of Geophysical Research* **117**(B4), 1–12.
URL: *http://www.agu.org/pubs/crossref/2012/2011JB008901.shtml*

Bath, M.: 1965, Lateral inhomogeneities of the upper mantle, *Tectonophysics* **2**(6), 483–514.

Beauval, C., Hainzl, S. and Scherbaum, F.: 2006, Probabilistic seismic hazard estimation in low-seismicity regions considering non-Poissonian seismic occurrence, *Geophysical Journal International* **164**(3), 543–550.
URL: *http://doi.wiley.com/10.1111/j.1365-246X.2006.02863.x*

Campbell, K. W. and Bozorgnia, Y.: 2008, NGA Ground Motion Model for the Geometric Mean Horizontal Component of PGA , PGV , PGD and 5 % Damped Linear Elastic Response Spectra for Periods Ranging from 0 . 01 to 10 s, *Earthquake Spectra* **24**(1), 139–171.

Cocco, M. and Rice, J. R.: 2002, Pore pressure and poroelasticity effects in Coulomb stress analysis of earthquake interactions, *Journal of Geophysical Research* **107**(B2).
URL: *http://www.agu.org/pubs/crossref/2002/2000JB000138.shtml*

Cohee, B. P. and Beroza, G. C.: 1994, Slip Distribution of the 1992 Landers Earthquake and Its Implications for Earthquake Source Mechanics, *Bulletin of the Seismological Society of America* **84**(3), 692–712.

Console, R., Murru, M. and Catalli, F.: 2006, Physical and stochastic models of earthquake clustering, *Tectonophysics* **417**(1-2), 141–153.
URL: *http://linkinghub.elsevier.com/retrieve/pii/S0040195105005767*

Console, R., Murru, M. and Lombardi, A. M.: 2003, Refining earthquake clustering models, *Journal of Geophysical Research* **108**(B10), 2468.

Cornell, C. A.: 1968, Engineering Seismic Risk Analysis, *Bulletin of the Seismological Society of America* **58**(5), 1583–1606.

Cotton, F. and Campillo, M.: 1995, Frequency domain inversion of strong motions: Application to the 1992 Landers earthquake, *Journal of Geophysical Research* **100**(B3), 3961–3975.

Custódio, S., Liu, P. and Archuleta, R. J.: 2005, The 2004 M w 6.0 Parkfield, California, earthquake: Inversion of near-source ground motion using multiple data sets, *Geophysical Research Letters* **32**(23), 10–13.
URL: *http://www.agu.org/pubs/crossref/2005/2005GL024417.shtml*

Dreger, D. S., Gee, L., Lombard, P., Murray, M. H. and Romanowicz, B.: 2005, Rapid Finite-source Analysis and Near-fault Strong Ground Motions: Application to the 2003 Mw 6.5 San Simeon and 2004 Mw6.0 Parkfield Earthquakes, *Seismological Research Letters* **76**(1), 40–48.

Dziewonski, A. M., Chou, T. A. and Woodhouse, J. H.: 1981, Determination of earthquake source parameters from waveform data for studies of global and regional seismicity, *Journal of Geophysical Research* **86**(B4), 2825.
URL: *http://doi.wiley.com/10.1029/JB086iB04p02825*

Ekström, G., Nettles, M. and Dziewonski, A. M.: 2012, The global CMT project 2004â2010: Centroid-moment tensors for 13,017 earthquakes, *Physics of the Earth and Planetary Interiors* **200-201**, 1–9.
URL: *http://linkinghub.elsevier.com/retrieve/pii/S0031920112000696*

Gerstenberger, M. C., Wiemer, S., Jones, L. M. and Reasenberg, P. A.: 2005, Real-time forecasts of tomorrow â s earthquakes in California, *Nature* **435**(May), 2–5.

Guo, Z. and Ogata, Y.: 1997, Statistical relations between the parameters of aftershocks in time, space, and magnitude, *Journal of Geophysical Research* **102**(B2), 2857–2873.
URL: *http://www.agu.org/pubs/crossref/1997/96JB02946.shtml*

Hainzl, S., Brietzke, G. B. and Zöller, G.: 2010, Quantitative earthquake forecasts resulting from static stress triggering, *Journal of Geophysical Research* **115**(B11), 1–9.
URL: *http://www.agu.org/pubs/crossref/2010/2010JB007473.shtml*

Hainzl, S., Christophersen, A. and Enescu, B.: 2008, Impact of Earthquake Rupture Extensions on Parameter Estimations of Point-Process Models, *Bulletin of the Seismological Society of America* **98**(4), 2066–2072.
URL: *http://www.bssaonline.org/cgi/doi/10.1785/0120070256*

Hainzl, S., Enescu, B., Cocco, M., Woessner, J., Catalli, F., Wang, R. and Roth, F.: 2009, Aftershock modeling based on uncertain stress calculations, *Journal of Geophysical Research* **114**(B5), 1–12.
URL: *http://www.agu.org/pubs/crossref/2009/2008JB006011.shtml*

Hainzl, S., Zakharova, O. and Marsan, D.: 2013, Impact of Aseismic Transients on the Estimation of Aftershock Productivity Parameters, *Bulletin of the Seismological Society of America* **103**(3), 1723–1732.
URL: *http://www.bssaonline.org/cgi/doi/10.1785/0120120247*

Hainzl, S., Zöller, G. and Wang, R.: 2010, Impact of the receiver fault distribution on aftershock activity, *Journal of Geophysical Research* **115**(B5), 1–12.
URL: *http://www.agu.org/pubs/crossref/2010/2008JB006224.shtml*

Hardebeck, J. L., Nazareth, J. J. and Hauksson, E.: 1998, The static stress change triggering model: Constraints from two southern California aftershock sequences, *Journal of Geophysical Research* **103**(B10), 427–437.

Harris, R. A.: 1998, Introduction to special section: Stress triggers, stress shadows, and implications for seismic hazard, *Journal of Geophysical Research* **103**(B10), 347–358.
URL: *http://www.agu.org/pubs/crossref/1998/98JB01576.shtml*

Hauksson, E., Yang, W. and Shearer, P. M.: 2012, Waveform Relocated Earthquake Catalog for Southern California (1981 to June 2011), *Bulletin of the Seismological Society of America* **102**(5), 2239–2244.
URL: *http://www.bssaonline.org/cgi/doi/10.1785/0120120010*

Helmstetter, A., Kagan, Y. Y. and Jackson, D. D.: 2005, Importance of small earthquakes for stress transfers and earthquake triggering, *Journal of Geophysical Research* **110**(B05S08).

Helmstetter, A., Kagan, Y. Y. and Jackson, D. D.: 2006, Comparison of Short-Term and Time-Independent Earthquake Forecast Models for Southern California, *Bulletin of the Seismological Society of America* **96**(1), 90–106.
URL: *http://bssa.geoscienceworld.org/cgi/doi/10.1785/0120050067*

Hernandez, B., Cotton, F. and Campillo, M.: 1999, Contribution of radar interferometry to a two-step inversion of the kinematic process of the 1992 Landers earthquake, *Journal of Geophysical Research* **104**(B6).

Herrero, A. and Bernard, P.: 1994, A Kinematic Self-Similar Rupture Process for Earthquakes, *Bulletin of the Seismological Society of America* **84**(4), 1216–1228.

Ji, C., King, K. K., Larson, K. M. and Hudnut, K. W.: 2004, Co-seismic slip history and early afterslip of the 2004 Parkfield earthquake, *AGU Fall Meeting Abstracts*.
URL: *http://adsabs.harvard.edu/abs/2004AGUFM.S53D..04J*

Ji, C., Wald, D. J. and Helmberger, D. V.: 2002a, Source Description of the 1999 Hector Mine, California, Earthquake, Part I: Wavelet Domain Inversion Theory and Resolution Analysis, *Bulletin of the Seismological Society of America* **92**(4), 1192–1207.
URL: *http://bssa.geoscienceworld.org/cgi/doi/10.1785/0120000916*

Ji, C., Wald, D. J. and Helmberger, D. V.: 2002b, Source Description of the 1999 Hector Mine, California, Earthquake, Part II : Complexity of Slip History, *Bulletin of the Seismological Society of America* **92**(4), 1208–1226.

King, G. C. P., Stein, R. S. and Lin, J.: 1994, Static Stress Changes and the Triggering of Earthquakes, *Bulletin of the Seismological Society of America* **84**(3), 935–953.
URL: *http://linkinghub.elsevier.com/retrieve/pii/0148906295944842*

Knopoff, L. and Gardner, J. K.: 1974, Is the sequence of earthquakes in southern California, with aftershocks removed, poissonian?, *Bulletin of the Seismological Society of America* **64**(5), 1363–1367.

Marsan, D.: 2003, Triggering of seismicity at short timescales following Californian earthquakes, *Journal of Geophysical Research* **108**, 1–14.

Marsan, D.: 2006, Can coseismic stress variability suppress seismicity shadows ? Insights from a rate-and-state friction model, *Journal of Geophysical Research* **111**, 1–11.

Marsan, D. and Lengliné, O.: 2008, Extending earthquakes' reach through cascading., *Science* **319**(5866), 1076–1079.
URL: *http://www.ncbi.nlm.nih.gov/pubmed/18292339*

McCloskey, J.: 2003, Structural constraints on the spatial distribution of aftershocks, *Geophysical Research Letters* **30**(12), 1610.
URL: *http://www.agu.org/pubs/crossref/2003/2003GL017225.shtml*

Nur, A. and Booker, J. R.: 1972, Aftershocks caused by pore fluid flow?, *Science* **175**(4024), 885–887.
URL: *http://www.ncbi.nlm.nih.gov/pubmed/17781062*

Ogata, Y.: 1983, Estimation of the Parameters in the Modified Omori Formula for Aftershock Frequencies by the Maximum Likelihood Procedure, *Journal of Physics of the Earth* **31**, 115–124.

Ogata, Y.: 1988, Statistical Models for Earthquake Occurrences and Residual Analysis for Point Processes, *Journal of the American Statistical Association* **83**(401), 9–27.

Ogata, Y.: 1998, Space-time Point-process Models for Earthquake Occurrences, *Ann. Inst. Statist. Math.* **50**(2), 379–402.

Okada, Y.: 1992, INTERNAL DEFORMATION DUE TO SHEAR AND TENSILE FAULTS IN A HALF-SPACE, *Bulletin of the Seismological Society of America* **82**(4), 1018–1040.

Perfettini, H. and Avouac, J.-P.: 2007, Modeling afterslip and aftershocks following the 1992 Landers earthquake, *Journal of Geophysical Research* **112**(B7), 1–19.
URL: *http://www.agu.org/pubs/crossref/2007/2006JB004399.shtml*

Salichon, J., Lundgren, P., Delouis, B. and Giardini, D.: 2004, Slip History of the 16 October 1999 Mw 7.1 Hector Mine Earthquake (California) from the Inversion of InSAR, GPS, and Teleseismic Data, *Bulletin of the Seismological Society of America* **94**(6), 2015–2027.

Steacy, S., Marsan, D., Nalbant, S. S. and McCloskey, J.: 2004, Sensitivity of static stress calculations to the earthquake slip distribution, *Journal of Geophysical Research* **109**(B4), 1–16.
URL: *http://www.agu.org/pubs/crossref/2004/2002JB002365.shtml*

Steacy, S., Nalbant, S. S., McCloskey, J., Nostro, C., Scotti, O. and Baumont, D.: 2005, Onto what planes should Coulomb stress perturbations be resolved?, *Journal of Geophysical Research* **110**(B5), 1–14.
URL: *http://www.agu.org/pubs/crossref/2005/2004JB003356.shtml*

Utsu, T., Ogata, Y. and Matsu'ura, R. S.: 1995, The Centenary of the Omori Formula for a Decay Law of Aftershock Activity, *Journal of Physics of the Earth* **43**, 1–33.

van der Elst, N. J. and Brodsky, E. E.: 2010, Connecting near-field and far-field earthquake triggering to dynamic strain, *Journal of Geophysical Research* **115**(B7), 1–21.
URL: *http://www.agu.org/pubs/crossref/2010/2009JB006681.shtml*

Wald, D. J. and Heaton, T. H.: 1994, Spatial and Temporal Distribution of Slip for the 1992 Landers, California, Earthquake, *Bulletin of the Seismological Society of America* **84**(3), 668–691.

Wald, D. J., Lin, K.-W. and Quitoriano, V.: 2008, Quantifying and Qualifying USGS ShakeMap Uncertainty, *Technical report*.

Wang, R., Lorenzo-Martín, F. and Roth, F.: 2006, PSGRN/PSCMP - a new code for calculating co- and post-seismic deformation, geoid and gravity changes based on the viscoelastic-gravitational dislocation theory, *Computers and Geosciences* **32**(4), 527–541.

Wells, D. L. and Coppersmith, K. J.: 1994, New Empirical Relationships among Magnitude , Rupture Length , Rupture Width , Rupture Area , and Surface Displacement, *Bulletin of the Seismological Society of America* **84**(4), 974–1002.

Werner, M. J., Helmstetter, A., Jackson, D. D. and Kagan, Y. Y.: 2011, High-Resolution Long-Term and Short-Term Earthquake Forecasts for California, *Bulletin of the Seismological Society of America* **101**(4), 1630–1648.

Woessner, J., Hainzl, S., Marzocchi, W., Werner, M. J., Lombardi, A. M., Catalli, F., Enescu, B., Cocco, M., Gerstenberger, M. C. and Wiemer, S.: 2011, A retrospective comparative forecast test on the 1992 Landers sequence, *Journal of Geophysical Research* **116**(B5), 1–22.
URL: *http://www.agu.org/pubs/crossref/2011/2010JB007846.shtml*

5 Appendix

5.1 Reference slip models

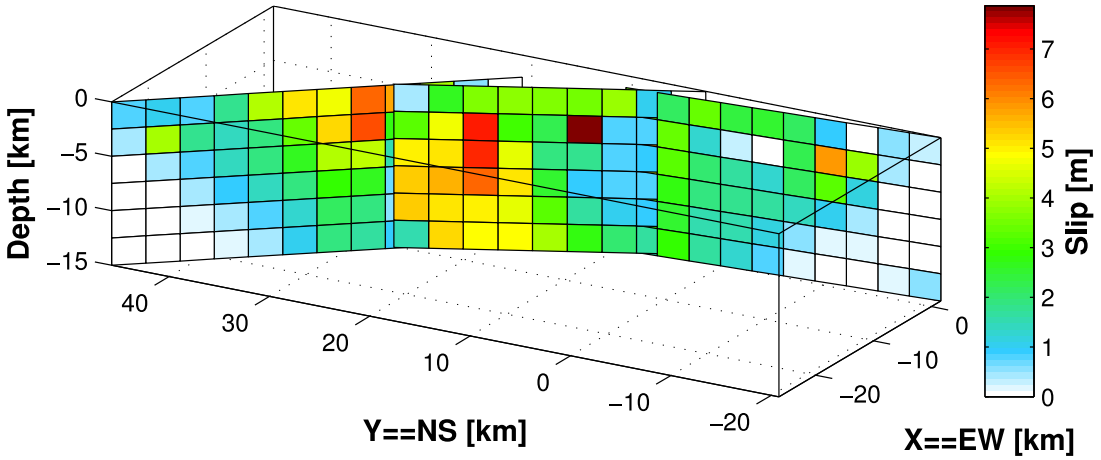

Figure 5.1: Landers Wald and Heaton (1994) slip model.

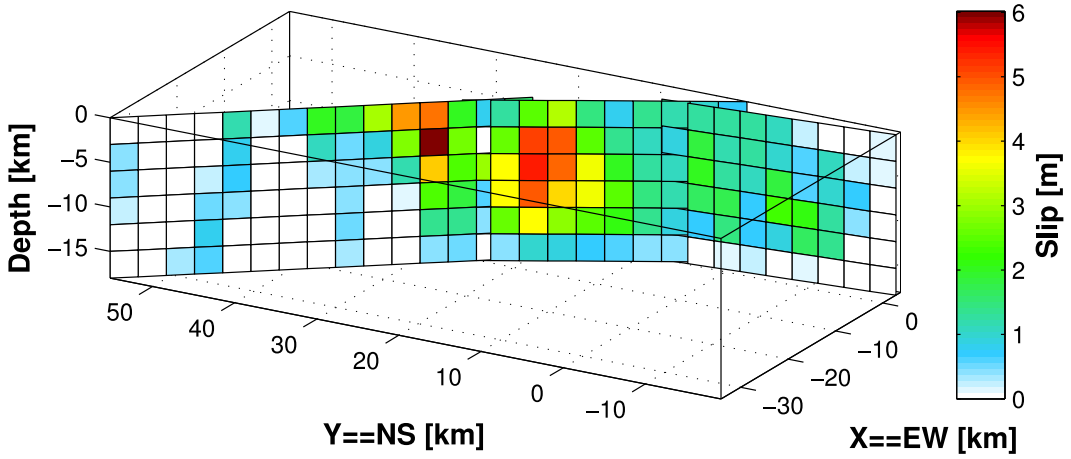

Figure 5.2: Landers Cohee and Beroza (1994) slip model.

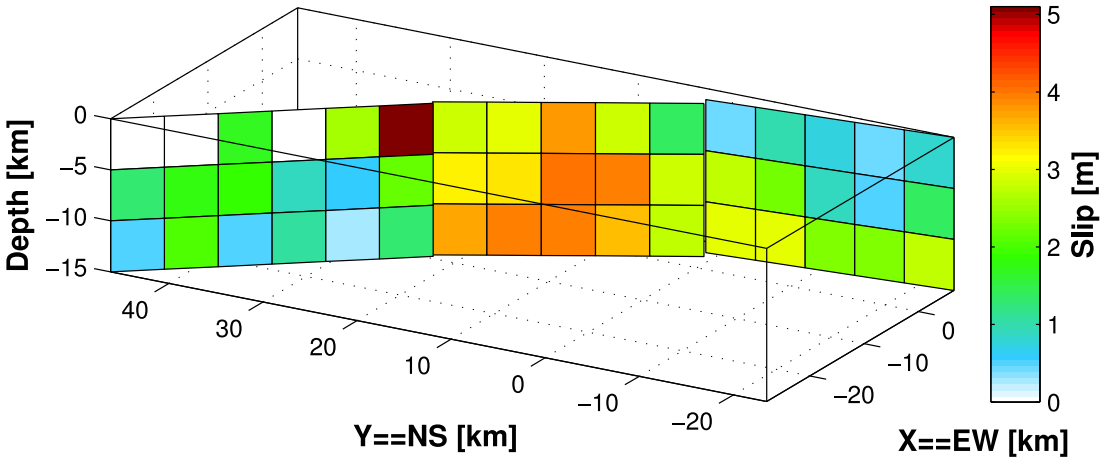

Figure 5.3: Landers Cotton and Campillo (1995) slip model.

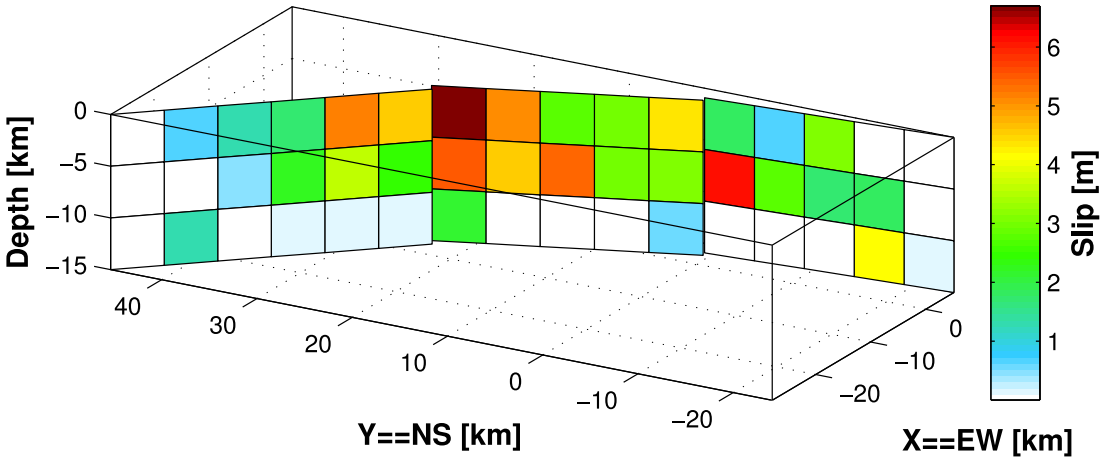

Figure 5.4: Landers Hernandez et al. (1999) slip model.

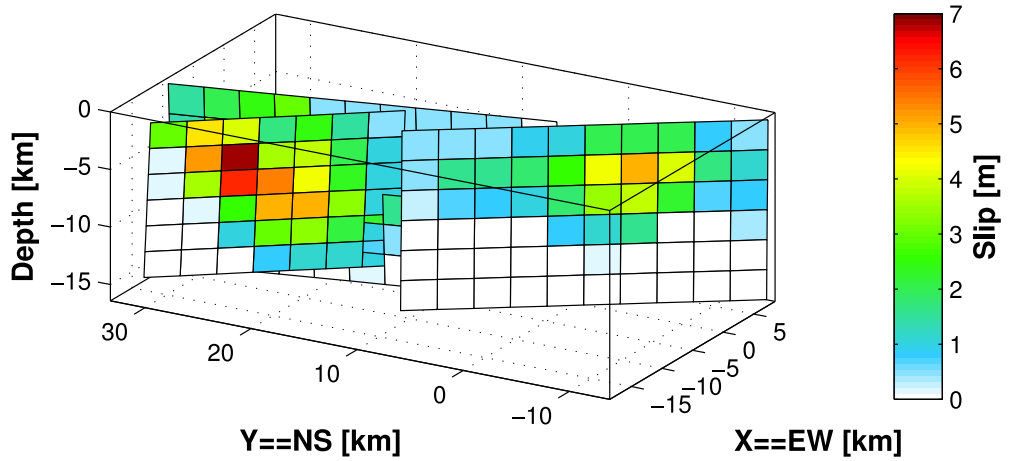

Figure 5.5: Hector Mine Ji et al. (2002a) slip model.

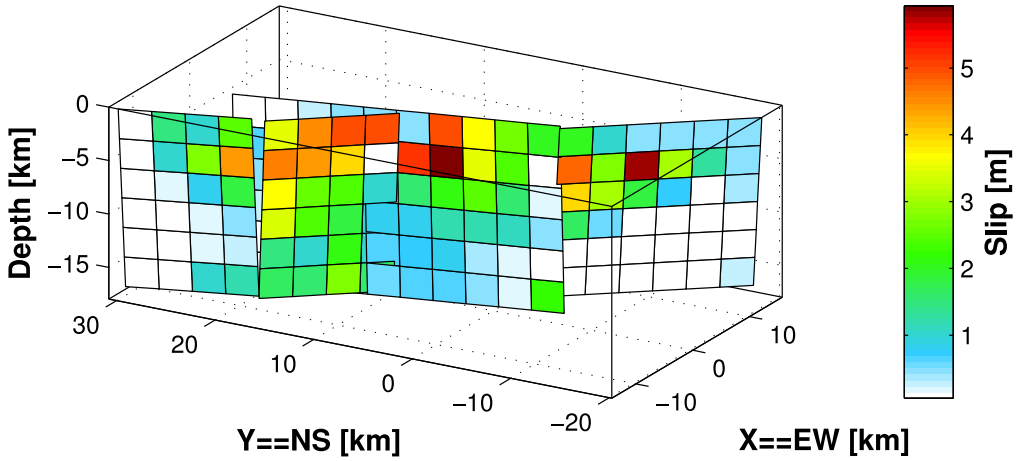

Figure 5.6: Hector Mine Salichon et al. (2004) slip model.

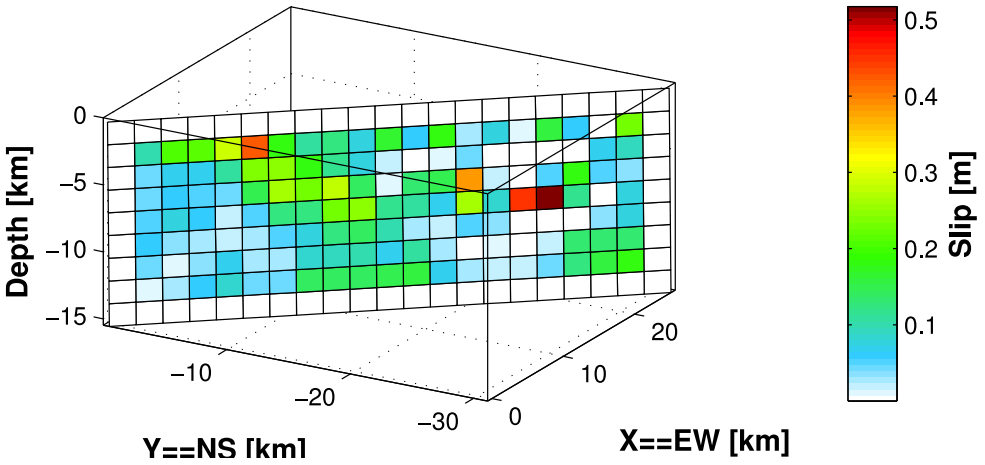

Figure 5.7: Parkfield Custódio et al. (2005) slip model.

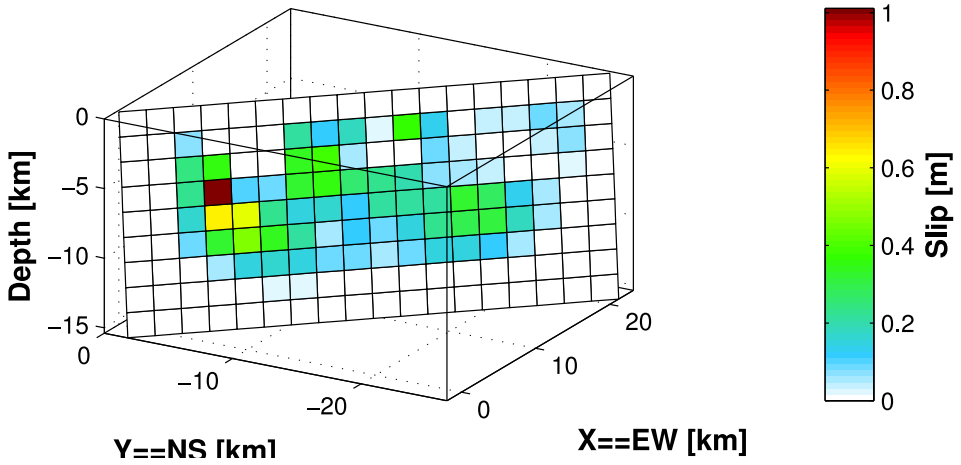

Figure 5.8: Parkfield Dreger et al. (2005) slip model.

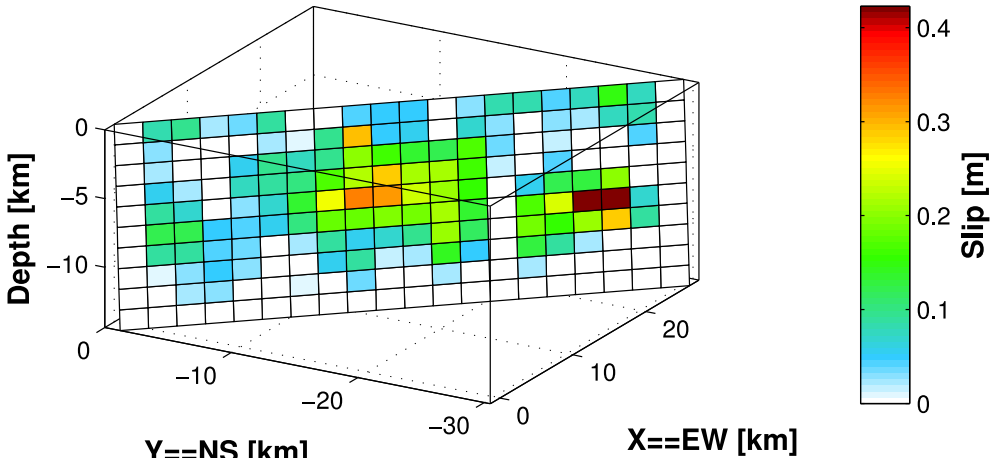

Figure 5.9: Parkfield Ji et al. (2004) slip model.

5.2 Stress based probability maps

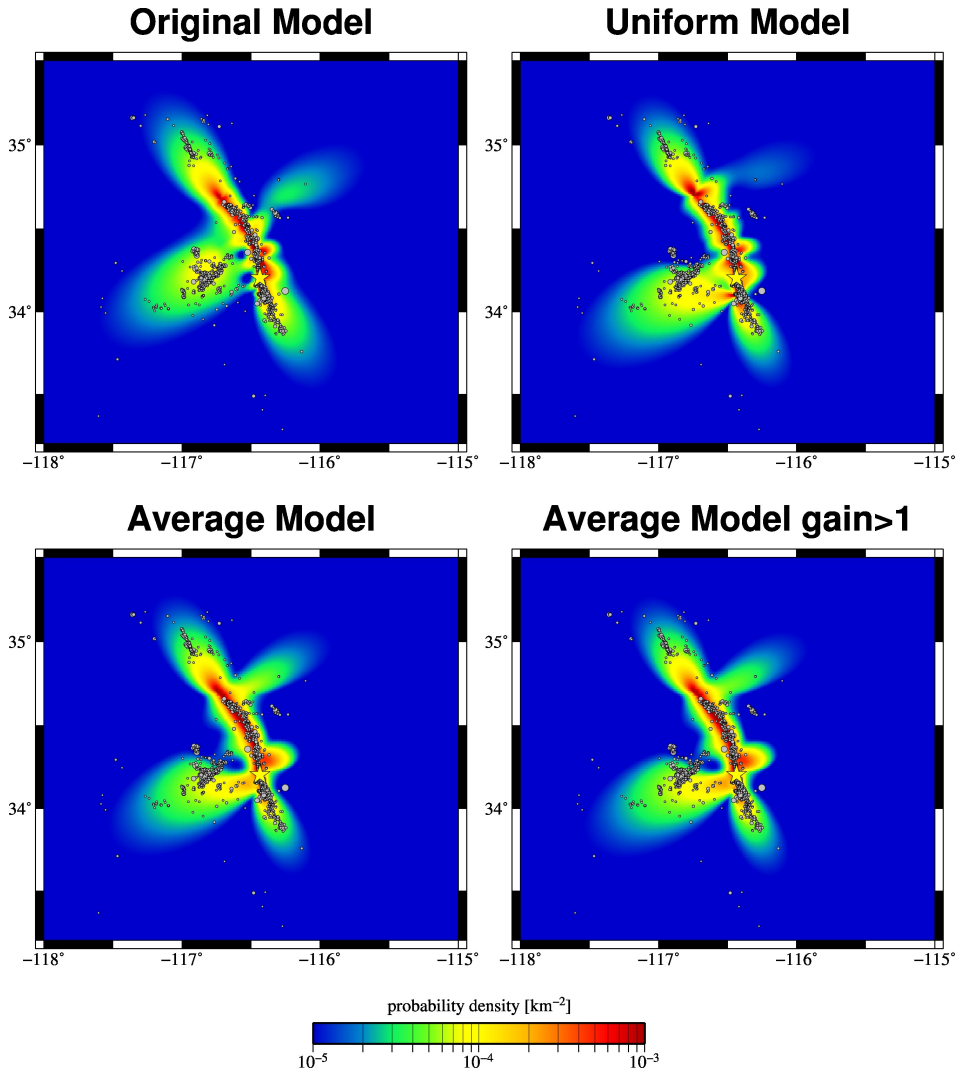

Figure 5.10: Landers Wald and Heaton (1994) probability distributions based on original slip model, uniform slip model, average slip model and average slip model (probability gain > 1).

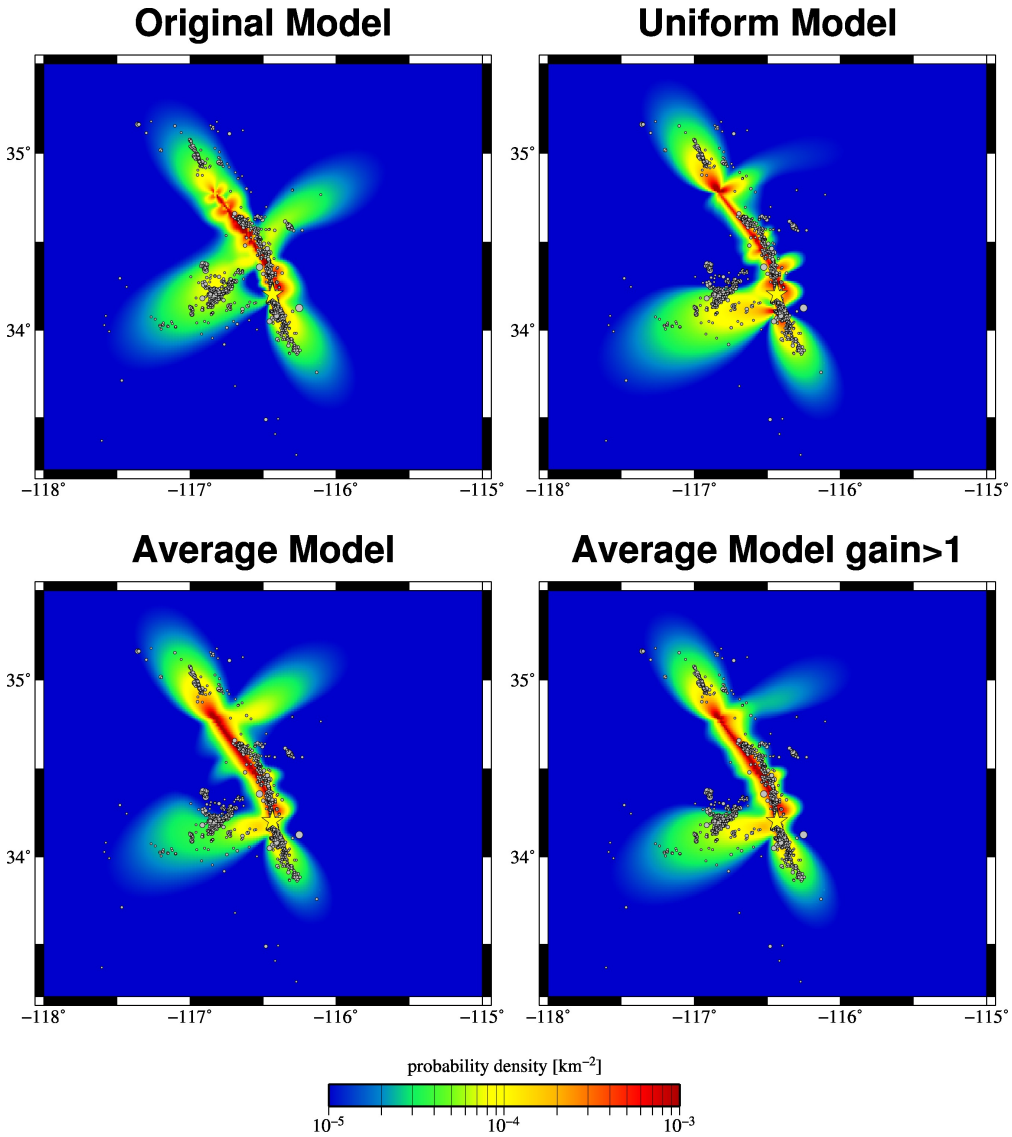

Figure 5.11: Landers Cohee and Beroza (1994) probability distributions based on original slip model, uniform slip model, average slip model and average slip model (probability gain > 1).

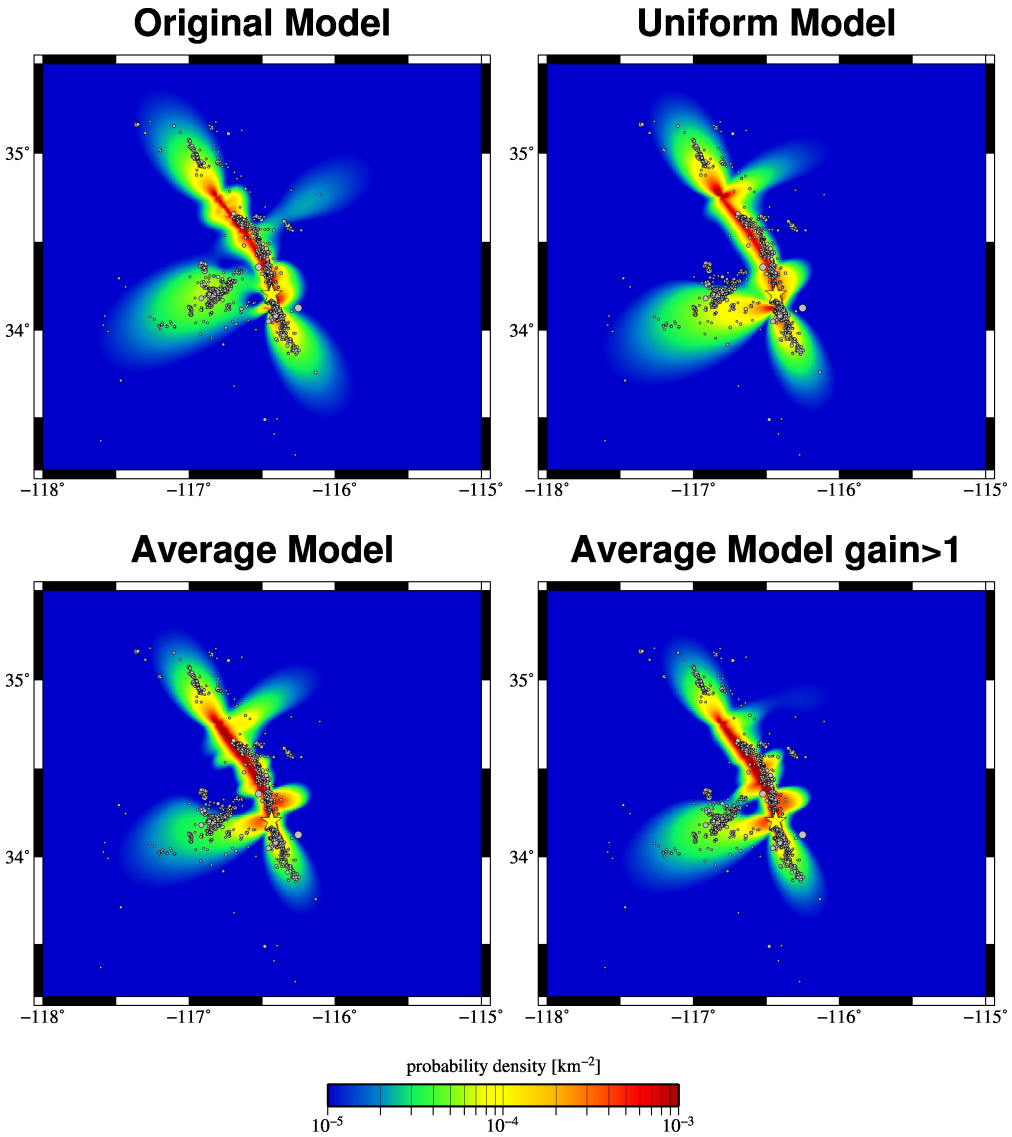

Figure 5.12: Landers Cotton and Campillo (1995) probability distributions based on original slip model, uniform slip model, average slip model and average slip model (probability gain > 1).

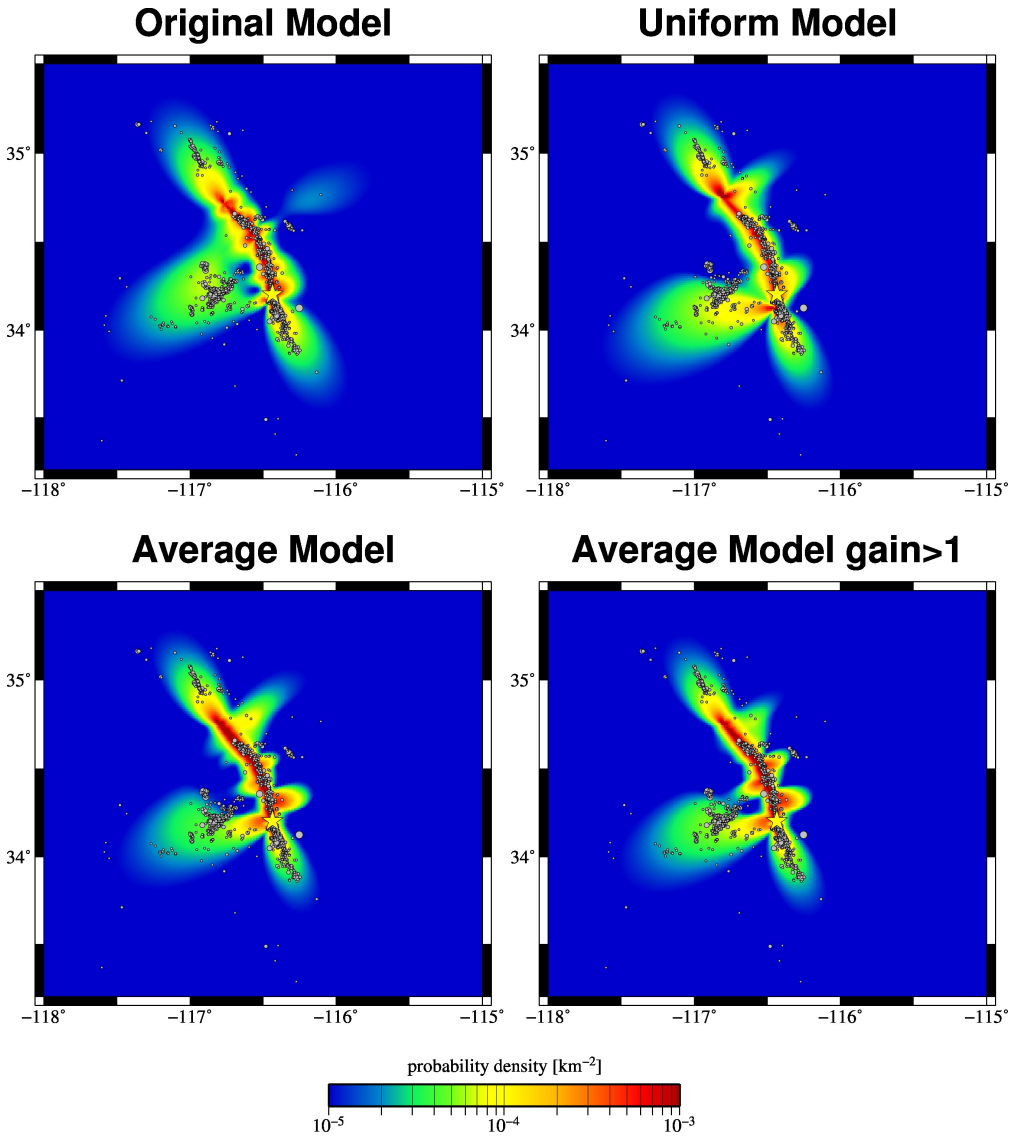

Figure 5.13: Landers Hernandez et al. (1999) probability distributions based on original slip model, uniform slip model, average slip model and average slip model (probability gain > 1).

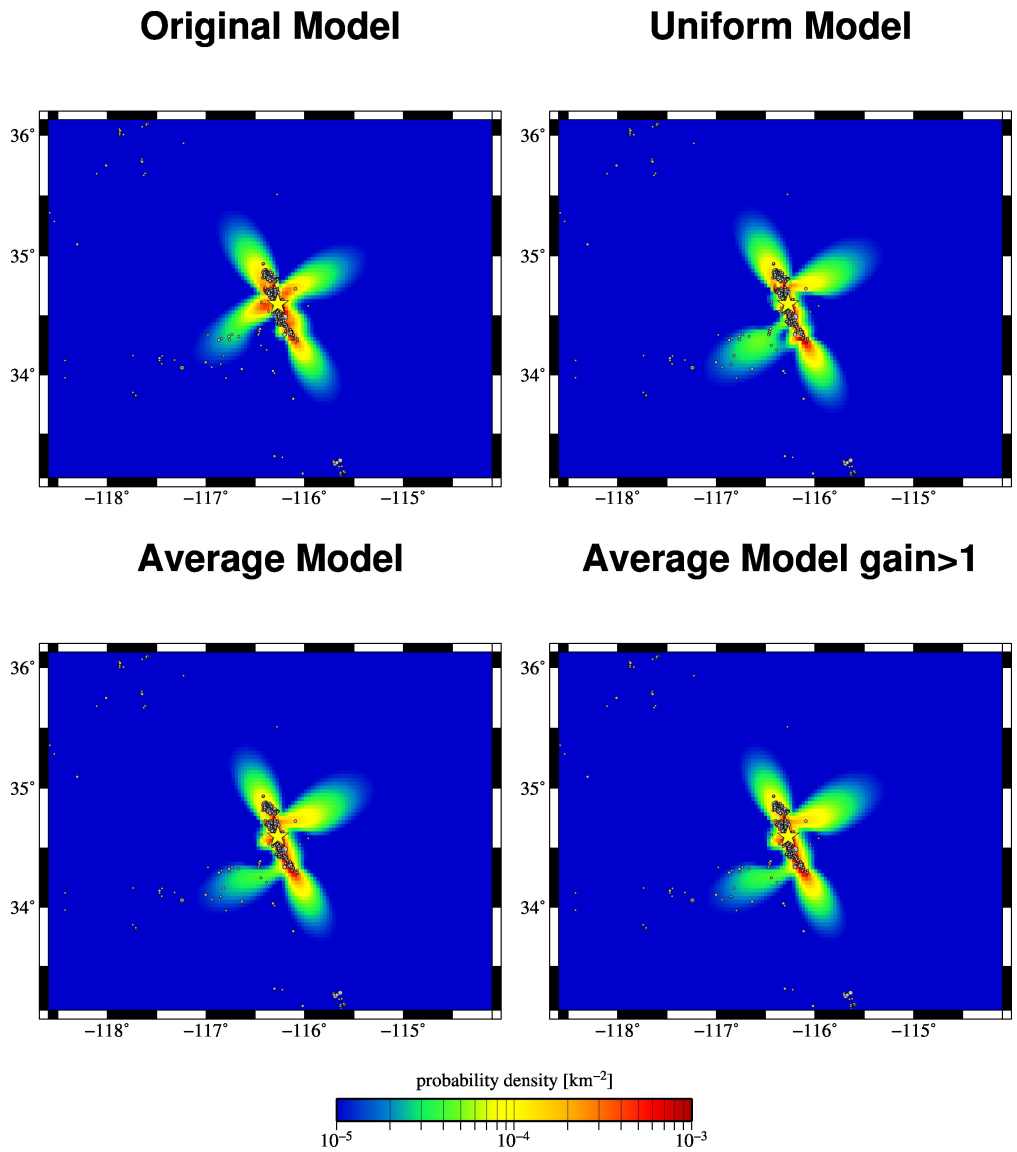

Figure 5.14: Hector Mine Ji et al. (2002a) probability distributions based on original slip model, uniform slip model, average slip model and average slip model (probability gain > 1).

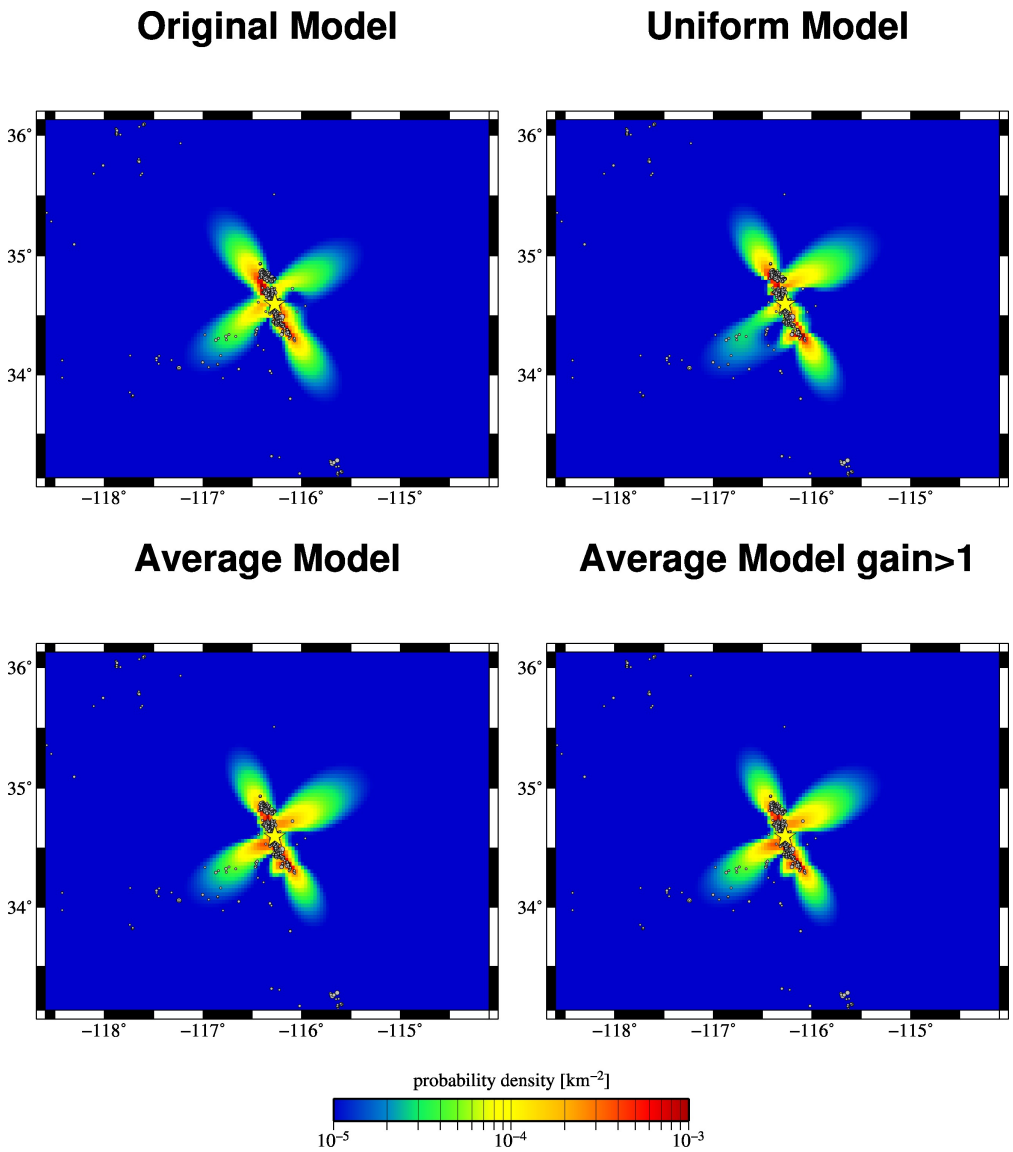

Figure 5.15: Hector Mine Salichon et al. (2004) probability distributions based on original slip model, uniform slip model, average slip model and average slip model (probability gain > 1).

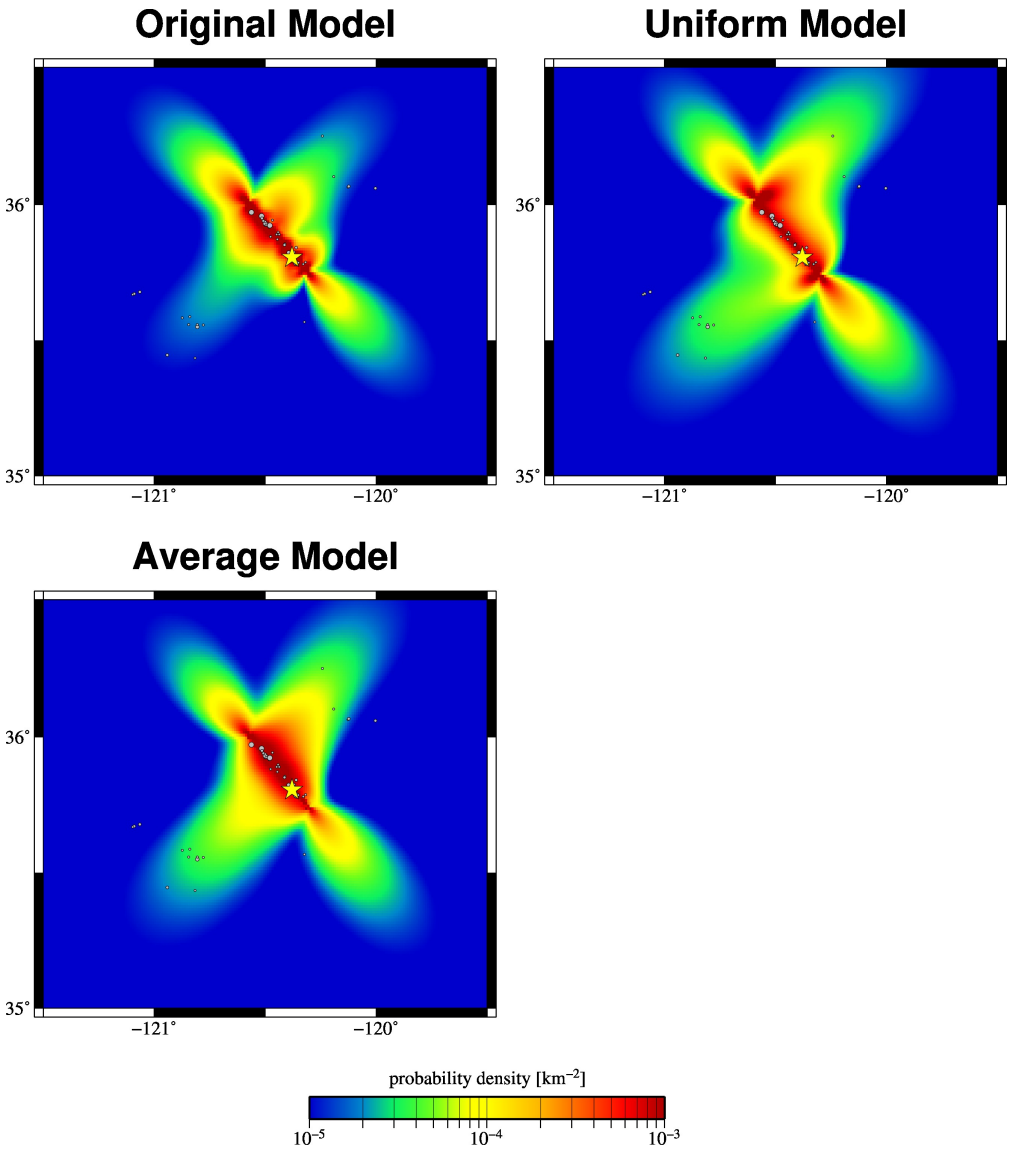

Figure 5.16: Parkfield Custódio et al. (2005) probability distributions based on original slip model, uniform slip model, average slip model and average slip model (probability gain > 1).

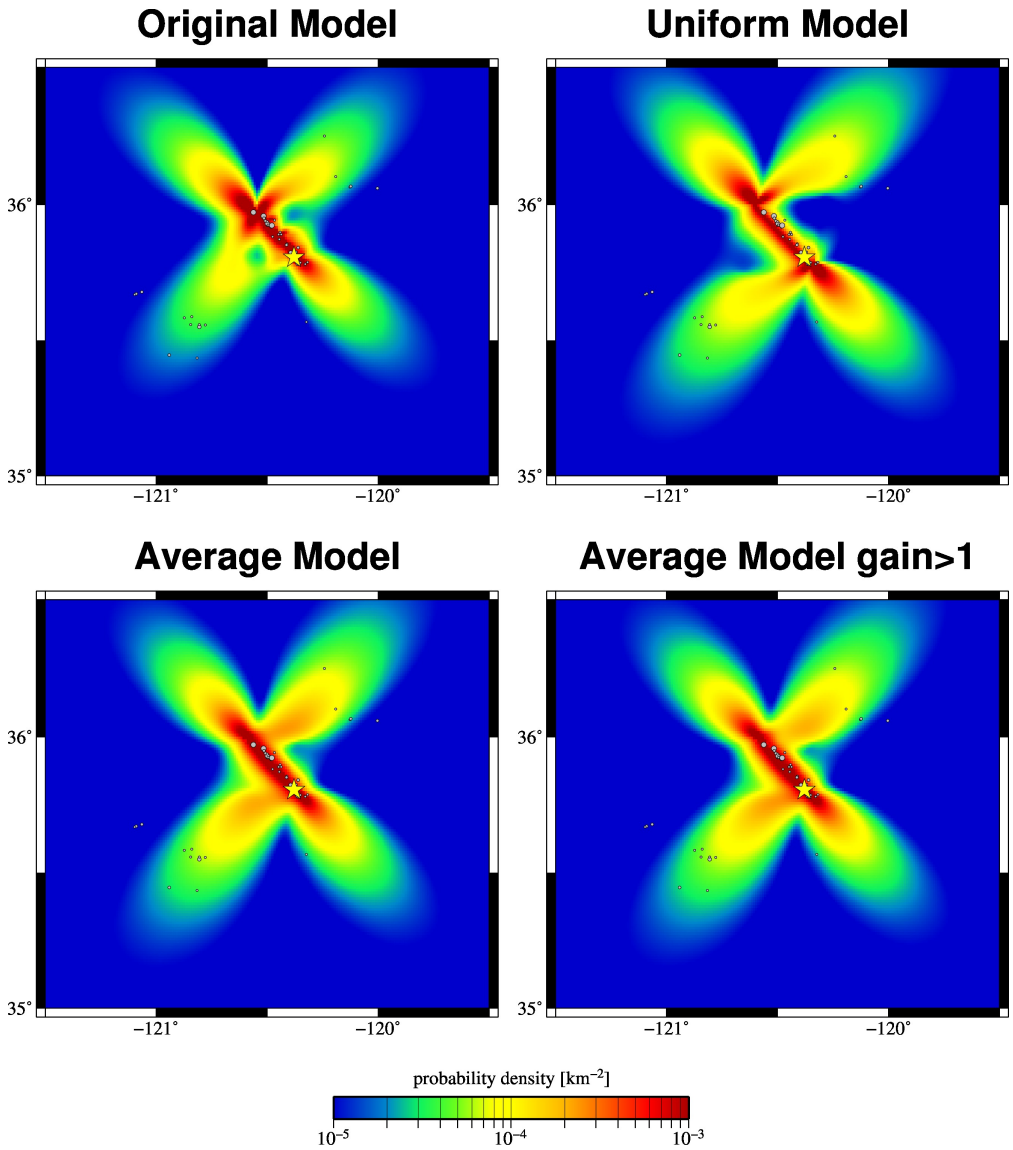

Figure 5.17: Parkfield Dreger et al. (2005) probability distributions based on original slip model, uniform slip model, average slip model and average slip model (probability gain > 1).

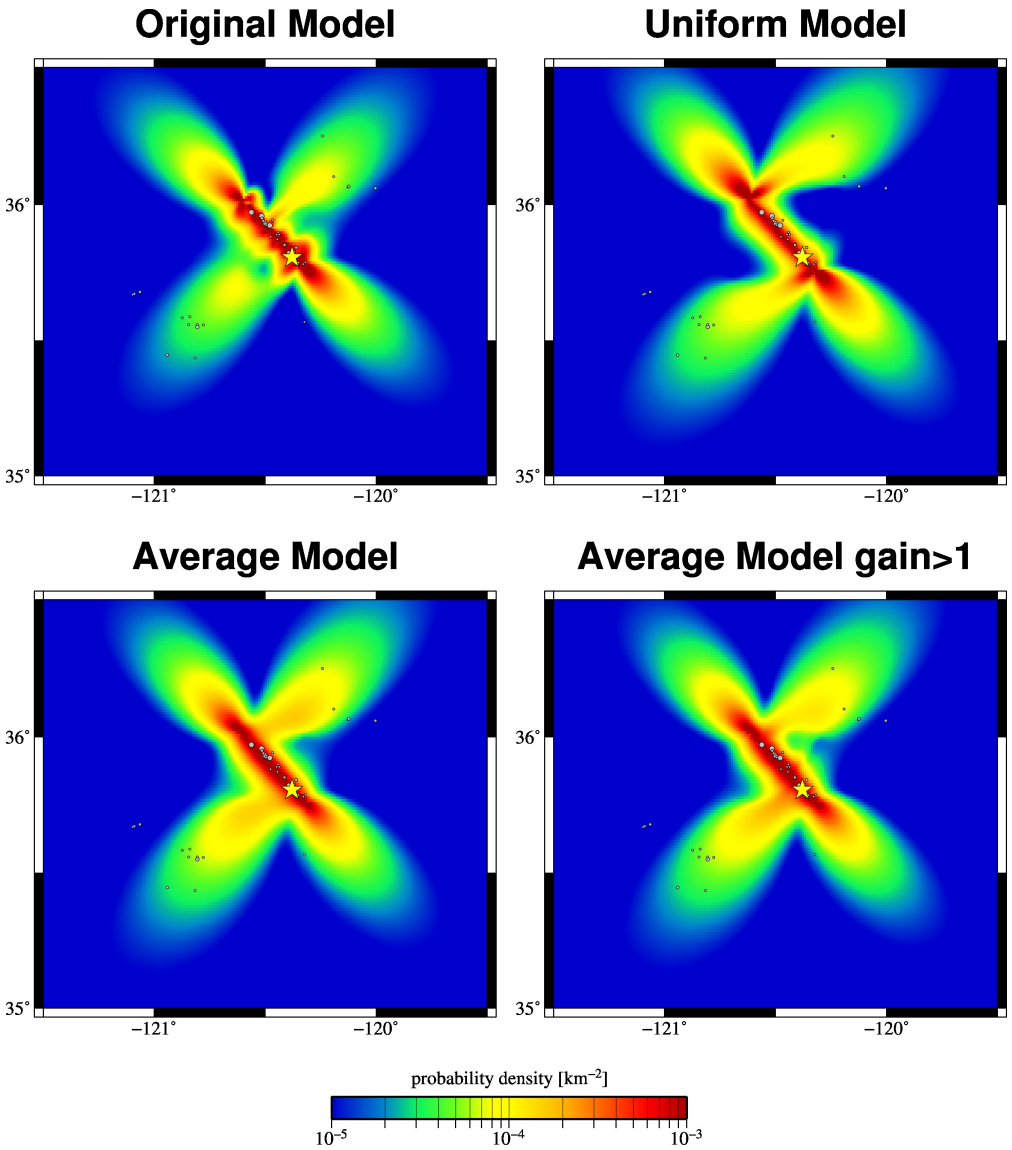

Figure 5.18: Parkfield Ji et al. (2004) probability distributions based on original slip model, uniform slip model, average slip model and average slip model (probability gain > 1).